https://doi.org/10.5194/egusphere-2026-1804
Preprint. Discussion started: 4 May 2026

Long-Term Decoupling of Precipitation Extremes from Mean Annual Precipitation During Repeated Early Paleogene Hyperthermals in the North American Mid-Latitudes

Jacob S. Slawson[1], Piret Plink-Bjorklund[1], Emily J. Beverly[2]

[1]Geology and Geological Engineering, Colorado School of Mines, Golden, 80401, United States
[2]School of Earth and Environmental Sciences, University of Minnesota Twin Cities, Minneapolis, 55455, United States

Correspondence to: Jacob Slawson (jslawson@mines.edu)

Abstract. The early Paleogene hyperthermals, including the Paleocene-Eocene Thermal Maximum and the hyperthermals of the Early Eocene Climatic Optimum, were the warmest periods of the Cenozoic Era. Due to the similar continental configuration and drivers of extreme warmth, this period serves as an analogue for how precipitation is altered by extreme warming driven by greenhouse gases. Through high resolution geochronology and construction of a bulk organic carbon isotope curve, we identify up to 11 different hyperthermals in the Uinta Basin, Utah, adding to the small number of terrestrial sites where the lower magnitude Paleocene and Eocene hyperthermals have been recognized. We use paleosol bulk geochemistry methods to quantify changes in precipitation during these extreme warming events. We find no significant changes in mean annual precipitation during the warming events. However, paleosol mass balance results track increased clay illuviation, accumulation of redox-sensitive elements, and carbonate leaching during many of these events. These results, along with shifts in fluvial stratigraphy, provide evidence for increased intensity and seasonality or intermittency of precipitation that may be related to poleward shifts in global circulation. These results are compared to the state-of-the-art DeepMIP model ensemble, composed of the same models used for future climate simulations. The model ensemble overestimates mean annual precipitation and underestimates the seasonality or intermittency of precipitation compared to this proxy record. These differences may be a function of the coarse model resolution, missing processes, or incorrect boundary conditions that should be investigated further.

1 Introduction

Climate change is expected to alter hydroclimate in the coming centuries. On a global scale, climate models show a wet-gets-wetter, dry-gets-drier response where the mid-latitudes are expected to become wetter and the subtropics drier (Cramwinckel et al., 2023; Held and Soden, 2006). On a regional and continental scale this response can be complicated by atmospheric circulation changes, such as latitudinal shifts in the storm tracks, especially when precipitation extremes are considered (Byrne and O'Gorman, 2015; Carmichael et al., 2018; Slawson et al., 2025a, b; Zhang et al., 2024). In Europe and North America, observational studies already indicate an increase in extreme precipitation events (Dittus et al., 2015;

Donat et al., 2019). Model studies suggest future increases of extreme precipitation, surpassing the Clausius-Clapeyron scaling, and decoupling of temperature increases from mean annual precipitation changes (Bao et al., 2017; Slawson et al., 2025a).

Given that dramatic increases in temperature are expected under even intermediate climate change scenarios, there is an increasing need to turn to the past to test models and inform about future climate (Burke et al., 2018; Tierney et al., 2020). The most extreme examples of greenhouse gas-induced warming and hydroclimate alterations in the last 60 million years occurred in the early Paleogene period (Carmichael et al., 2017; Mcinerney and Wing, 2011; Zachos et al., 2008). The early Paleogene is characterized by the warmest temperatures of the Cenozoic Era with superimposed rapid global warming events or hyperthermals (Cramer et al., 2003; Littler et al., 2014; Westerhold et al., 2018, 2020; Zachos et al., 2008) . The best known hyperthermal is the Paleocene-Eocene Thermal Maximum (PETM) 55.9 to 55.7 Ma, caused by the largest carbon release of the Cenozoic era, leading to global temperatures with estimates up to ~18°C warmer than the preindustrial mean (Inglis et al., 2020; Mcinerney and Wing, 2011). The PETM was followed by the Early Eocene Climatic Optimum (EECO) from 53.26 to 49.14 Ma (Westerhold et al., 2018). The EECO is characterized by the warmest sustained temperatures of the Cenozoic Era and a series of superimposed hyperthermals (Lauretano et al., 2015, 2018; Westerhold et al., 2018; Zachos et al., 2008), making it a good temperature analogue for the worst case climate change scenarios in the coming centuries (Burke et al., 2018). In addition, the EECO is favorable for climate studies due to the similar continental configuration (Matthews et al., 2016), availability of terrestrial proxies in multiple sedimentary basins (e.g. Foreman et al., 2012; Hyland et al., 2018; Kraus et al., 2013), and large-scale modeling studies (e.g. Cramwinckel et al., 2023; Lunt et al., 2021; Williams et al., 2022).

The Uinta Basin, located in northeastern Utah, USA, contains a terrestrial record of the early Paleogene in a 1000 m section of fluvial and lacustrine strata (Birgenheier et al., 2020; Slawson et al., 2025b). Previous work identifies the PETM in the Uinta Basin and demonstrates decoupling of precipitation intensity and intermittency from mean annual precipitation (MAP), possibly linked to the moisture transport capability and seasonality of the North American Monsoon (Slawson et al., 2025b). Other studies of the PETM have also noted similarly complex changes in hydroclimate (e.g. Foreman et al., 2012; Payros et al., 2022; Schmitz & Pujalte, 2007), but relatively little is known about the drivers of these changes or the response of hydroclimate to the lower magnitude hyperthermals. Here we explore the response of hydroclimate to the more extreme hyperthermals, such as the PETM, and the lower magnitude hyperthermals of the late Paleocene and early Eocene (Westerhold et al., 2018; Zachos et al., 2008). We use paleosol-based bulk geochemical proxies and a mass-balance approach to quantify mean annual precipitation (MAP) and changes in chemical weathering throughout the early Paleogene period, spanning approximately ten million years. Negative carbon isotope excursions (NCIEs) together with magnetostratigraphy and absolute age dates are used to identify the hyperthermals. These results are compared to other proxy records in the US Intermountain West and the DeepMIP ensemble results from the newly available web-based application (Steinig et al., 2024) to compare model performance and assess potential atmospheric drivers of spatial shifts in precipitation.

1.1 Geologic setting

The Uinta Basin is an asymmetric, intermountain basin spanning central and northern Utah into northwestern Colorado over an area of 20,000 km^2 (Figure 1) (Dickinson et al., 1988). It was formed during the Laramide Orogeny from the Late Cretaceous to Eocene as part of a series of intermountain sedimentary basins (Dickinson et al., 1988). The basin is bound by the Laramide Uinta Mountains to the north, San Rafael Swell to the southwest, Douglas Creek Arch to the east, and the eastern terminus of the Sevier Orogeny to the west (Figure 1) (Dickinson et al., 1988). This study focuses on the Colton/Wasatch and Green River Formations. The term "Colton Formation" is typically used to describe the fluvial deposits west of the present-day Green River (Spieker, 1946) and "Wasatch Formation" east of the Green River (Hayden, 1869). The Colton/Wasatch Formation is a dominantly fluvial wedge interpreted as a fluvial fan deposited by the variable discharge California Paleoriver from the late Paleocene to the early Eocene (Carraro et al., 2023; Dickinson et al., 2012; Jones, 2017; Plink-Björklund et al., 2014). Both terms refer to one genetically related lobate wedge of dominantly fluvial deposits. For simplicity and to match the terminology of other recent publications (Carraro et al., 2023), we use "Wasatch Formation" hereafter.

The Wasatch Formation can be divided into two major types of deposits. Floodplain mudstone deposits are brown to red and include immature to moderately developed paleosols, which alternate vertically and laterally with fine to medium grained lenticular sandstones and amalgamated sandstones, interpreted as main trunk channel and crevasse splay deposits (Carraro et al., 2023; Jones, 2017). Age control of the Wasatch Formation is provided by biostratigraphy (Fouch et al., 1987) and magnetostratigraphy (Slawson et al., 2025b) (Figure 1). Previous work identifies the PETM as a 43 m fluvial section marked by a lithologic shift to amalgamated channel sandstones and mud clast conglomerates, dominated by upper flow regime sedimentary structures, and sandier paleosols that persisted for 70 m beyond the end of the CIE (Plink-Björklund et al., 2014; Slawson et al., 2025b).

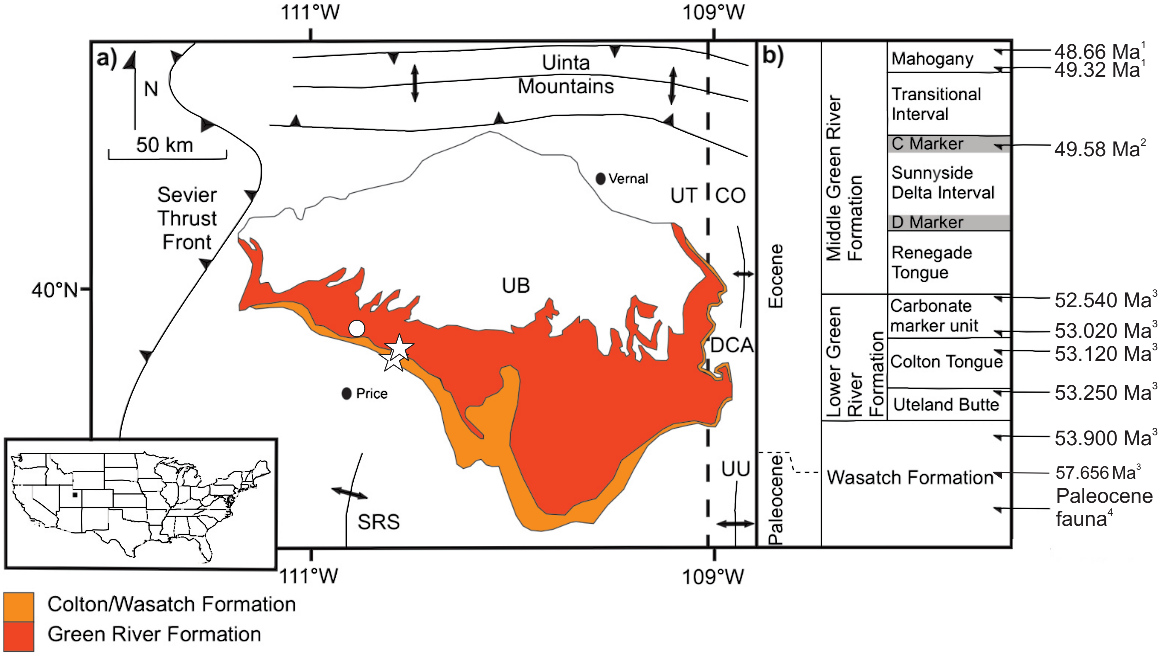

Figure 1: (a) Map showing the exposure of the Colton/Wasatch (orange) and Green River Formations (red) in the Uinta Basin. The white stars mark the locations where samples were collected in Nine Mile Canyon, and the white circle indicates the sampling locations in roadcuts along highway 191. The black square in the inset map marks the location of the Uinta Basin relative to the United States. Map abbreviations: SRS: San Rafael Swell; DCA: Douglas Creek Arch; UU: Uncompahgre Uplift. Modified from Fouch et al. (1987), Dickinson et al. (2012), and Wang and Plink-Bjorklund (2019). (b) Stratigraphic column showing the formation names, stratigraphic markers, and their ages based on absolute age dates with sources noted by superscripts ([1]Smith et al., 2010, [2]Smith & Carroll, 2015), magnetostratigraphy ([3]Slawson et al., 2025b, using reversals with ages from Ogg, 2020), and biostratigraphy ([4]Fouch et al., 1987).

The Green River Formation is a mixed fluvial-lacustrine deposits where dominantly fluvial facies transition to lacustrine facies further north in the deeper portion of the basin (Birgenheier et al., 2020; Fouch et al., 1994). The Green River Formation is subdivided into three informal units: the lower, middle, and upper (Figure 1). This designation is relative to the lacustrine intervals, including the Uteland Butte, the Carbonate Marker Unit, and the Mahogany Oil Shale, where the Uteland Butte marks the beginning of the lower Green River Formation, and the Carbonate Marker Unit and Mahogany Oil Shale mark the top of the lower and middle Green River Formation, respectively (Figure 1) (Fouch et al., 1987; Fouch, 1975; Remy, 1992). The lacustrine intervals are separated by fluvial units known as the Colton Tongue, the Renegade Tongue, and the Sunnyside Delta Interval. Age control of the Green River Formation is constrained by magnetostratigraphy (Slawson et al., 2025b) and absolute age dates in the C Marker (49.58 ± 0.28 Ma) and at the base and top of the Mahogany Interval (49.32 ± 0.30 and 48.66 ± 0.23 Ma; Figure 1). Similar to the Wasatch Formation, previous work has led to the identification of the fluvial units as a series of fluvial fans (Plink-Björklund et al., 2014; Wang & Plink-Bjorklund, 2019).This study will focus on the fluvial portions of these formations deposited in the central and western Uinta Basin and exposed in both Nine Mile Canyon and along the highway 191, about 10 km northeast of the town of Price, Utah (Figure 1).

The fluvial successions of the lower and middle Green River Formation are composed of similar deposits to the Wasatch Formation. The floodplain mudstone deposits are yellow-brown to red and similarly include immature to moderately developed paleosols that are commonly reduced (green-gray) at the base and top. These alternate vertically and laterally with fine to medium grained sandstones of channel and crevasse splay deposits (Birgenheier et al., 2020; Wang & Plink-Bjorklund, 2019). The Green River lacustrine units are composed of carbonate siltstones and grainstones, lacustrine siliciclastics and mixed facies, interfingered with deltaic deposits (Birgenheier et al., 2020; Melstrom and Birgenheier, 2021).

2 Materials and methods

2.1 Field methods

Two composite sections were created through physical correlation of the Wasatch Formation in a continuous cliff, and correlation of the Green River Formation along marker beds between Nine Mile Canyon and US Highway 191 (Figure 2) (Morgan, 2003). Samples from the Wasatch Formation through the Colton Tongue of the lower Green River Formation were collected in Nine Mile Canyon. The remainder of the samples in the middle Green River Formation were collected from exposures along US Highway 191 for easier sampling access. The stratigraphic sections were measured using a Jacob's Staff, and the paleosols and floodplain facies were trenched to obtain unweathered samples for bulk geochemistry and stable isotopic analysis. Paleosol morphologic descriptions are based on grain size, redoximorphic features, abundance and type of nodules, and presence/absence of vertic features using a standard soil description (Scheffe et al., 2015) and a Munsell soil color scheme (Munsell Color (Firm), 2010).

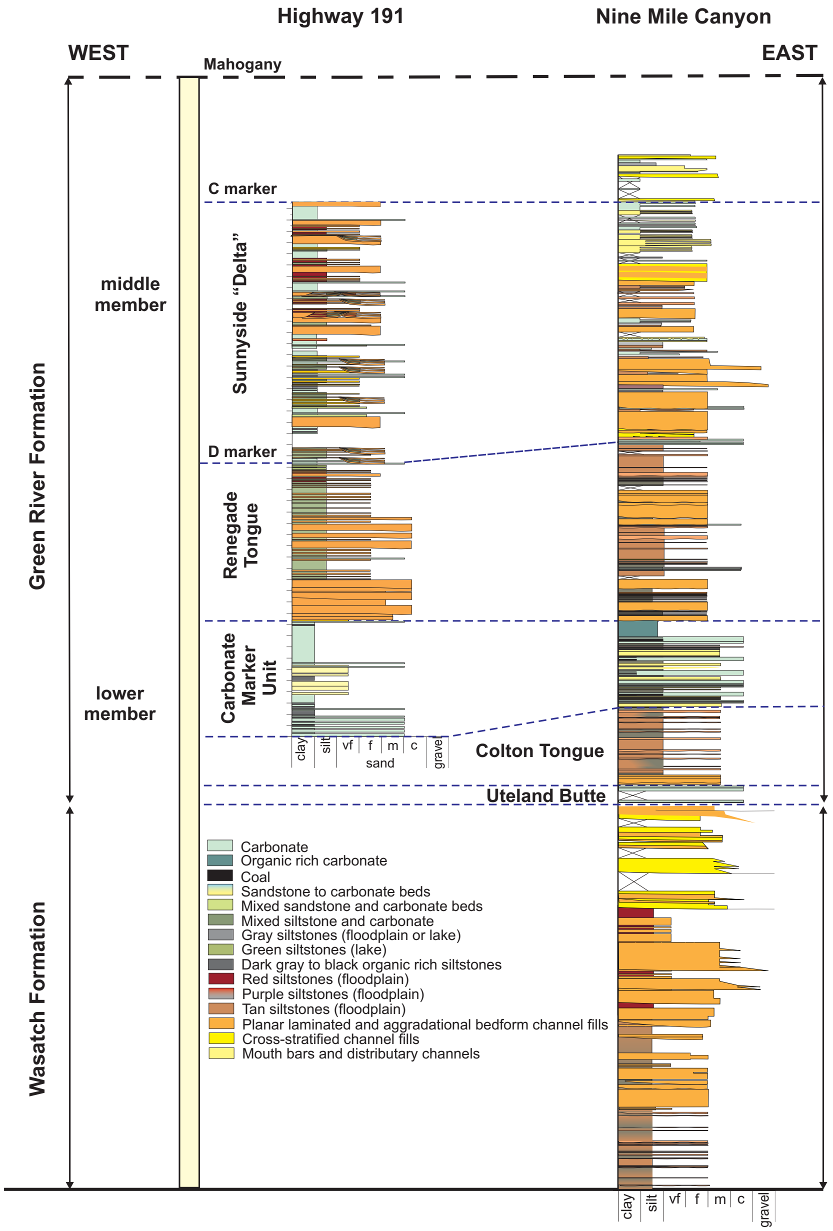

Figure 2: Correlated measured sections collected in Nine Mile Canyon and US Highway 191. Sampling was completed in Nine Mile Canyon through the Colton Tongue and at the US Highway 191 outcrops from the Renegade Tongue and Sunnyside Delta intervals.

2.2 Paleosol methods

In the floodplain sections, samples were collected from each paleosol, and both weathered (B-horizon) and unweathered parent materials were sampled for geochemical comparisons (Figure 3). Morphologic indicators such as ped development, soil horizons, and composite or compound soil profiles (Kraus, 1999) were used to assess whether the soils were developed enough to be considered in equilibrium with climate. Composite paleosols containing relict bedding were likely buried before they could be equilibrated with climate (Kraus et al., 2013; Stinchcomb et al., 2016), and thick, cumulative paleosols were likely exposed at the surface for too long and thus overprinted by multiple climate states (Kraus, 1999). Therefore, bulk geochemical proxies for paleosols with these features were not included in paleoclimate reconstructions.

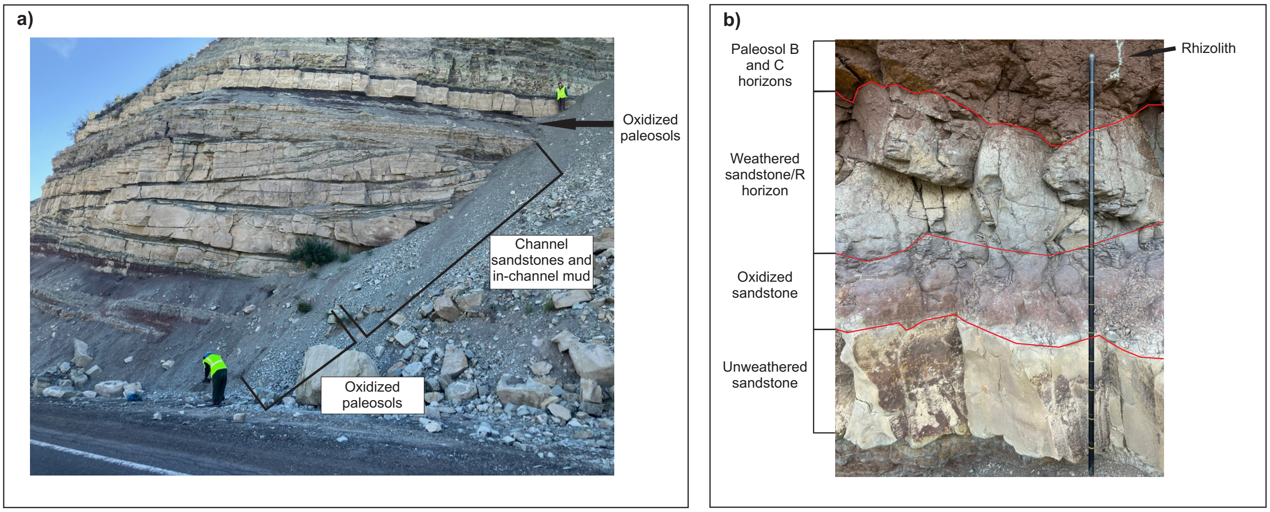

Figure 3: Representative photos fluvial and floodplain environments from the Uinta Basin. a) An outcrop of channel sandstones, in-channel muds, and paleosols from the Green River Formation. b) An oxidized paleosol with a rhizohalo from the Green River Formation, overlying a partially oxidized fluvial channel.

The samples were finely ground using a tungsten-carbide ring mill at Colorado School of Mines and commercially analyzed for major element oxides via X-ray fluorescence at ALS Geochemistry. Three paleosol-based proxies: 1) CIA-K (Sheldon et al., 2002), 2) $PPM_{1.0}$ (Stinchcomb et al., 2016), and 3) RF-MAP 2.0 (Lukens et al., 2019), were applied to reconstruct MAP throughout the early Paleogene. Additionally, constitutive mass-balance (τ) was performed to understand changes in elemental concentrations (*C)* between the weathered material (*w*) and the unweather parent material (*p*) in an immobile (*i*) element and element of interest (*j*). This technique provides a more nuanced understanding of the relationship between climate and soil development because it compensates for changes in parent material (Anderson et al., 2002; Brantley and Lebedeva, 2011; Brimhall and Dietrich, 1987). The τ of an element of interest (*j*) is calculated as:

$$\tau_j = \frac{C_{j,w}}{C_{j,p}}\frac{C_{i,p}}{C_{i,w}} - 1 \tag{1}$$

and when $\tau = -1$ there has been 100% depletion of the element and where $\tau > 0$ additions have occurred.

Potential parent materials were evaluated using plots of oxides and ratios of TiO_2, ZrO_2, and Al_2O_3 of parent materials and paleosols. The deviation between the parent and weathered material should be relatively small for immobile elements like Ti, Zr, Si, and Al (Maynard, 1992; White et al., 2008). Titanium is generally the preferred element because of its greater abundance in soils compared to Zr (wt % vs ppm) (Sheldon and Tabor, 2009; Stiles et al., 2003). Aluminum is generally not preferred because it is mobile under certain soil forming conditions (Ashley and Driese, 2000; Beverly et al., 2014).

2.3 Carbon isotope stratigraphy

The NCIEs that mark the hyperthermals are commonly located in fluvial stratigraphy using carbon isotopes of bulk organic material in floodplain sediments ($\delta^{13}C_{BOM}$) (e.g. Foreman et al., 2012; Schmitz & Pujalte, 2007). Samples were collected from floodplain sediments at 0.5 m resolution wherever possible. Approximately 20 mg of powdered sample was loaded into individual glass vials and treated with ten mL of 10% HCl until all inorganic carbon was removed. Samples were then washed with Milli-Q water until they reached a neutral pH and then were dried in an oven at 55°C. The dried samples were weighed into tin capsules and analyzed on an elemental-analyzer isotope ratio mass spectrometer at the Stable Isotope Laboratory at University of Colorado Boulder. The results were corrected based on comparison to in-house standards and are reported in δ-notation relative to the VPBD standard. The analytical standard deviation is ±0.36‰ based on comparison to in-house standards, and replicate analysis resulted in a standard deviation of ±0.28‰.

$\delta^{13}C_{BOM}$ records in terrestrial environments contain greater variation than marine isotopic records due to changes in plant community composition, sediment transport processes, and/or microbial activity (Baczynski et al., 2013; Foreman et al., 2012; Smith et al., 2007). Therefore, data are reported as both individual measurements and as a five-point rolling average; however, raw data is available in Table S1 and Figure S1. Values < -18‰ were not included in the five point rolling average (n = 15) because they are unrealistically heavy for C_3 plants that would have existed at this time (Arens et al., 2000; Kohn, 2010). These values are likely a result of samples that were not fully acidified and thus still contained inorganic carbon at the time of combustion (Könitzer et al., 2012).

3 Results

3.1 Paleosol morphology

The paleosols in the Wasatch and Green River Formations are relatively immature and range from paleo-Inceptisols to paleo-Vertisols (Figure 4). Normal grading from very fine sand in the R-horizon to sandy silt in C-horizon and clayey silt in the B-horizon is commonly observed. No A-horizons were observed, as is common in the geologic record (Beverly et al., 2018; Myers et al., 2014). The paleosols have subangular to angular blocky peds and in rare cases wedge peds. In places, channel sandstones were altered to form deep red paleosols. Seven major categories of paleosols, or pedotypes, are recognized (Figure 4 and Table 1) and classified following USDA Soil Taxonomy (Scheffe et al., 2015). Pedotypes A-D occur both in the Wasatch and Green River Formations, while Pedotypes F and G are unique to the Green River Formation. Pedotypes B and E are more common at stratigraphically higher intervals within the Wasatch Formation, beginning at the PETM onset (Figure 5c) (Slawson et al., 2025b). Pedotypes A-D are common throughout the first 150 m of section, and the rest of the Wasatch Formation is dominated by Pedotypes E and B which remain a deeper red (hue 10R) and coarser grained.

The Green River Formation paleosols differ from the underlying Wasatch paleosols in that they are primarily composed of Pedotypes F and G, and paleo-Vertisols are slightly more common (Figure 5c). No vertical trends were observed within the Green River Formation.

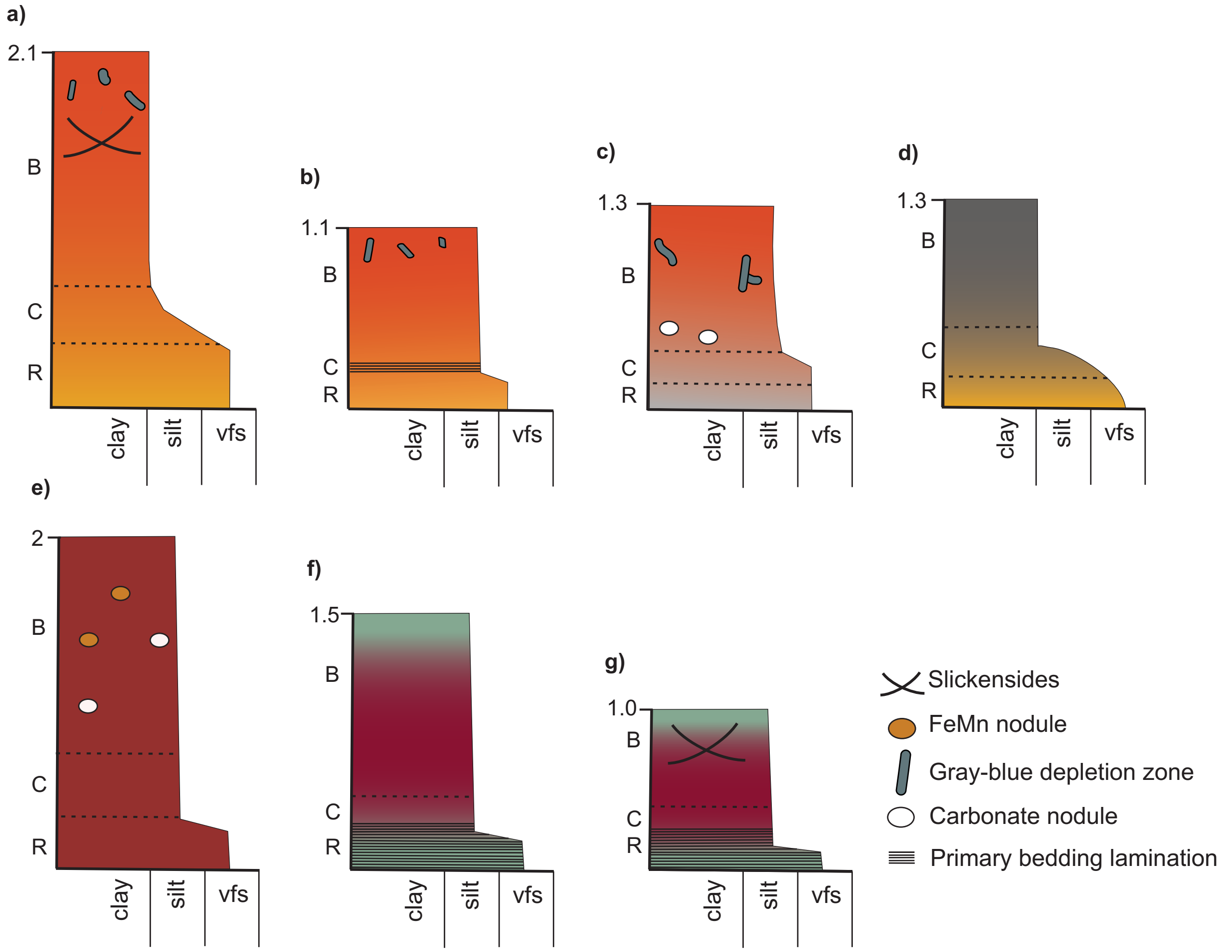

190 **Figure 4: Representative measured sections of Pedotypes A to G. a) Red-brown paleo-Vertisol with minor gray-blue redoximorphic features; b) Red-brown paleo-Inceptisol with laminated relict bedding in the C-horizon; c) Red paleo-Inceptisol with carbonate nodules and gray-blue redoximorphic features; d) Gray-brown, clay-rich paleo-Inceptisol; e) Deep red, sandy paleo-Inceptisol with carbonate nodules and FeMn nodules; f) Deep red paleo-Inceptisol with a gleyed upper B-, C-, and R-horizon; g) Deep red paleo-Vertisol with a gleyed upper B-, C-, and R- horizon.**

https://doi.org/10.5194/egusphere-2026-1804
Preprint. Discussion started: 4 May 2026

195 **Table 1. Summary of the pedotype characteristics and the interpreted soil types.**

	Munsell Color	**Observations**	**Soil Type**	**Paleoclimate Interpretation**
Pedotype A	2.5YR 4/4 (reddish brown)	Red-brown, clay-rich, slickensides, wedge texture, and occasional carbonate nodules.	Paleo-Vertisol	Dry, oxidizing conditions with a seasonal change in soil moisture.
Pedotype B	2.5R 4/4 (reddish brown)	Red-brown, silty, and angular blocky peds. No carbonate nodules.	Paleo-Inceptisol	Dry, oxidizing conditions.
Pedotype C	2.5YR 3/4 (reddish brown to dark reddish brown)	Red-brown, silty, subangular to angular blocky texture, and carbonate nodules	Paleo-Inceptisol	Dry, oxidizing conditions.
Pedotype D	5YR 4/3 (dark reddish gray to reddish brown)	Gray-brown, clay-rich, subangular to angular blocky texture. No carbonate nodules.	Paleo-Inceptisol	Dry, oxidizing conditions.
Pedotype E	10R 3/6 (dark red)	Deep red, very fine sand to sandy silt, subangular to angular blocky texture, and yellow-brown nodules.	Paleo-Inceptisol	Dry, oxidizing conditions with a seasonal change in soil moisture.
Pedotype F	10R 3/6 (dark red)	Deep red, very fine sand to clayey silt, and subangular to angular blocky texture. No carbonate nodules.	Paleo-Inceptisol	Dry, oxidizing conditions.
Pedotype G	10R 3/6 (dark red)	Deep red, grey-green at the top and base ,very fine sand to clayey silt, and wedge texture. No carbonate nodules.	Paleo-Vertisol	Dry, oxidizing conditions with a seasonal change in soil moisture.

Pedotype A is a red-brown (2.5YR), clay-rich soil forming on top of tan, very fine sandstones (Figure 4a and Table 1). The uppermost B-horizon is marked by slickensides and minor zones of gray-blue redoximorphic features showing a downward tapering structure. Carbonate nodules are rarely observed in these paleosols. Due to the high abundance of smectitic clay and slickensides, these paleosols are identified as paleo-Vertisols (Mack et al., 1993; Retallack et al., 1993).

Pedotype B is a red-brown (2.5R) and coarser grained soil than Pedotype A (Figure 4b and Table 1), consisting of dominantly silt sized particles. It typically has C- and R- horizons of laminated mudstone or very fine sandstone. There are no pedogenic features aside from angular blocky peds in the B-horizon. Due to poor development and no evidence of vertic features, these paleosols are identified as paleo-Inceptisols (Mack et al., 1993; Retallack et al., 1993).

Pedotype C has a similar grain size to Pedotype B that grades from very fine sand in the C- and R- horizons to silt in the B-horizon. The paleosols have a red-brown hue of 2.5YR (Figure 4c and Table 1). These paleosols are slightly more developed than Pedotype B, commonly containing carbonate nodules and downward tapering zones of gray-blue redoximorphic features. The B-horizons commonly show subangular to angular blocky peds with relict bedding in the C-horizon. The lack of vertic features and relatively minor presence of carbonate nodules (<5%) leads us to identify these paleosols as paleo-Inceptisols (Mack et al., 1993; Retallack et al., 1993).

Pedotype D is clay-rich and typically has a gray-brown (hue 5YR) colored B-horizon (Figure 4d and Table 1). It is composed of angular to subangular blocky peds, but no other pedogenic features were observed. The gray-brown color and presence of clay may be indicative of slightly greater pedogenesis than the other pedotypes. Due to the lack of pedogenic features observed in these paleosols, they are identified as paleo-Inceptisols (Mack et al., 1993; Retallack et al., 1993).

Pedotype E comprises the coarsest paleosols observed (Figure 4e and Table 1) with very fine sand grading upward to sandy silt in the B-horizon. Subangular to angular blocky peds were commonly observed with laminated relict bedding in C-horizons. These paleosols are deep red (hue 10R) and commonly have yellow-brown nodules and minor carbonate nodules throughout the thick B-horizons. Similar to the other pedotypes, the coarse grain size and presence of easily weatherable minerals has led to the identification of these paleosols as paleo-Inceptisols (Mack et al., 1993; Retallack et al., 1993), although the presence of nodules indicates greater pedogenesis that in the other paleo-Inceptisols.

Pedotype F grades from very fine sand in the C- and R- horizons to clayey silt in the B-horizon (Figure 4f and Table 1). Subangular and angular blocky peds were common with laminated relict bedding in the C-horizon. Similar in color to Pedotype E, they are a deep red (hue 10R) in the center of the soil. However, the lower ~0.25m and upper ~0.25m of the paleosols are often gleyed and exhibit a green-gray color (gley 1, pale green). The lack of pedogenic features has led us to identify these as paleo-Inceptisols (Mack et al., 1993; Retallack et al., 1993).

Pedotype G is very similar to Pedotype F but is composed of wedge peds (Figure 4g and Table 1). The C- and R-horizons grade from very fine sand to laminated silt. The B-horizon is composed of a clayey silt that is presumably rich in smectitic clays given the presence of wedge peds. Slickensides were not readily observed, but the wedge peds are vertic features, leading us to identify these soils as paleo-Vertisols (Mack et al., 1993; Retallack et al., 1993).

3.2 Carbon isotopes and stratigraphy

$\delta^{13}C_{BOM}$ results from 375 samples and a five-point rolling average from the Wasatch to middle Green River Formations are plotted below alongside a measured section from Nine Mile Canyon and the corresponding age data (Figure 5b). The $\delta^{13}C_{BOM}$ averages -21.6‰ and ranges from -18‰ to -29.20‰ with values between -18‰ and -19‰ common between 300 and 500 m and 850 and 900 m. No data between 500-700 m and 720-830 m is due to lithologic changes (lacustrine deposits and thick amalgamated channel sandstones) or covered section (Figures 2 and 5).

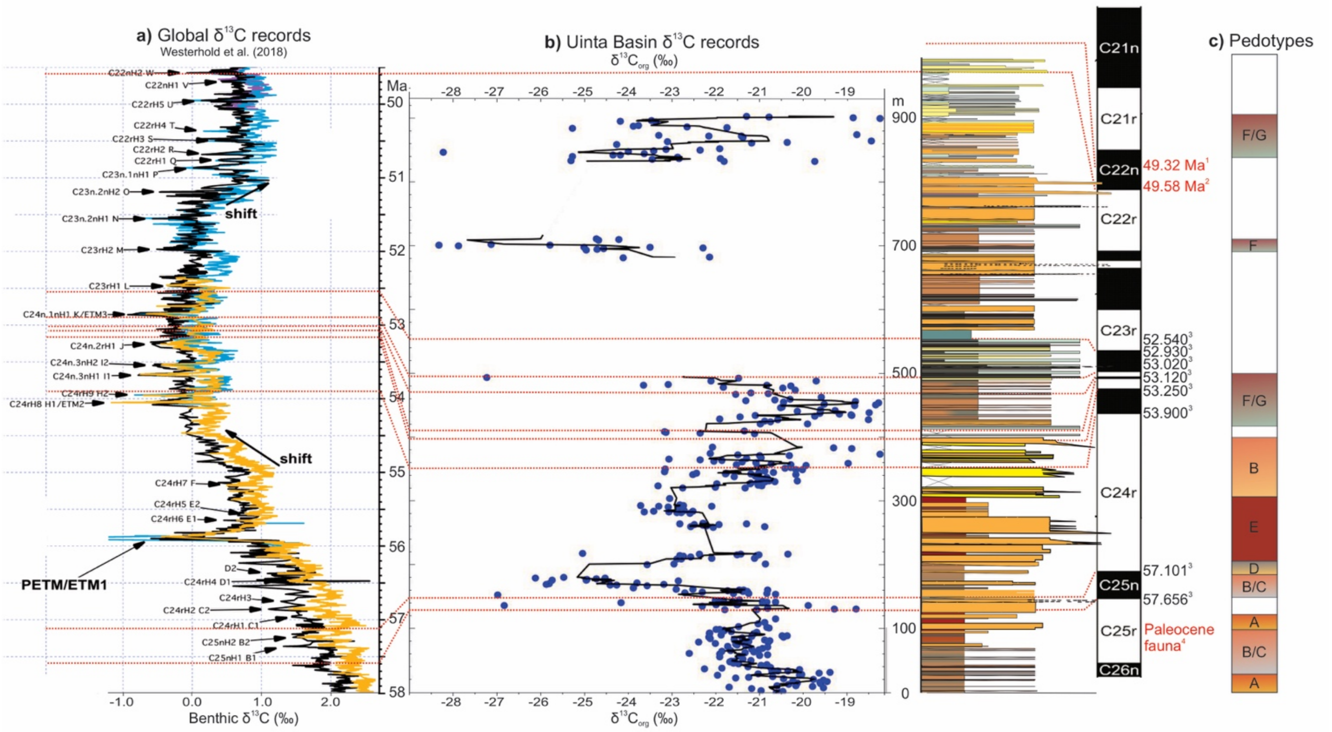

Figure 5: a) Global stable carbon isotopes and interpreted hyperthermals from Westerhold et al. (2018). The yellow and blue curves represent comparison to other Ocean Drilling Program cores, and the black curve is the curve described in the text and used for comparison; b) Stable carbon isotope results and five-point rolling average plotted alongside the Nine Mile Canyon measured section and age control. The Wasatch-Green River Formation contact is at approximately 395 m. Superscripts refer to [1]Smith et al. (2010), [2]Smith & Carroll (2015), [3]Slawson et al. (2025b), and [4]Fouch et al. (1987). Chron ages were provided in Ogg (2020); c) Simplified measured section detailing the common pedotypes throughout the stratigraphy.

3.3 Mean annual precipitation estimates

The mean annual precipitation estimates result from the three climofunctions, CIA-K, RF-MAP$_{2.0}$, and PPM$_{1.0}$, are shown for 53 paleosols (Figure 6, Table S2) (Sheldon et al., 2002; (Lukens et al., 2019; Stinchcomb et al., 2016). Mean annual precipitation (MAP) ranges between 300 and 1200 mm yr^{-1}, 300 to 1100 mm yr^{-1}, and 5 to 1300 mm yr^{-1} with average values of 595 ± 51 mm yr^{-1}, 441 ± 30 mm yr^{-1}, and 414 ± 66 mm yr^{-1} for the CIA-K, RF-MAP$_{2.0}$, and PPM$_{1.0}$ models, respectively. All three models indicate arid to sub-humid conditions throughout the Paleogene and show a brief increase in MAP at 115, 165, 300, and 425 m, but these increases are within proxy error, with the exception of the anomalously wet paleosol at 115

m. No long-term trends were observed.

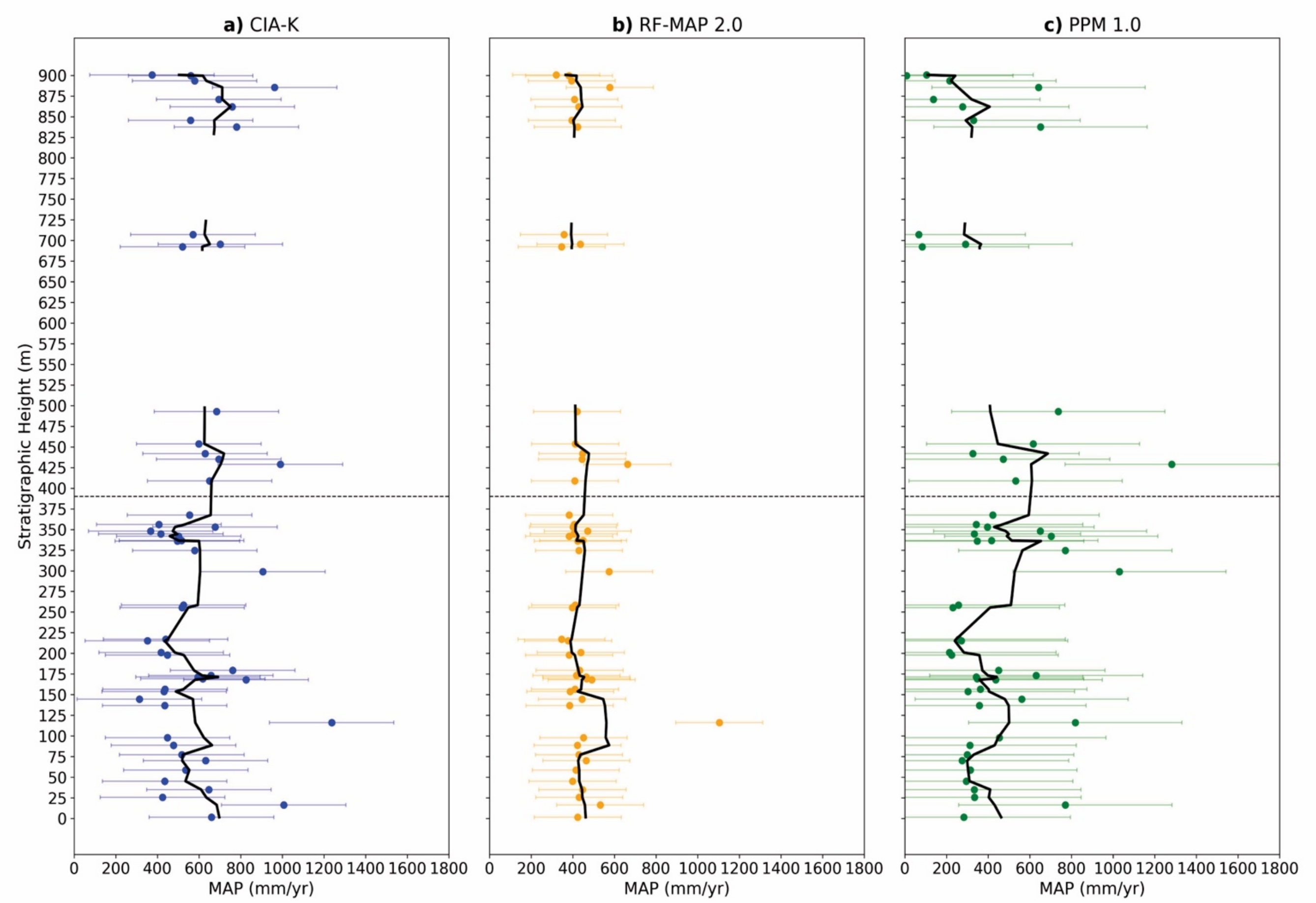

255 **Figure 6: Mean annual precipitation estimates based on bulk soil geochemistry results from a) Chemical Index of Alteration minus Potassium (CIA-K) (Sheldon et al., 2002), b) Random Forest Mean Annual Precipitation 2.0 (RF-MAP 2.0) (Lukens et al., 2019), and c) Paleosol Paleoclimate Model 1.0 (PPM$_{1.0}$) (Stinchcomb et al., 2016). The associated root mean square predictive errors are plotted as 299 mm yr^{-1}, 209 mm yr^{-1}, and 512 mm yr^{-1}, respectively (Lukens et al., 2019; Stinchcomb et al., 2016).**

3.4 Mass-balance geochemistry

3.4.1 Parent material identification

260 Unweathered parent materials of the paleosols range from laminated mudstones to very fine sandstones. In the Wasatch Formation, one very fine sandstone and two mudstones were collected from 153.3 m, 44.7 m, and 352.5 m. In the Green River Formation, similar grain size samples were collected from 441.5 m, 692.2 m, and 885.2 m. It was not possible to collect and analyze every potential parent material, and therefore, these samples are used as representative parent materials for paleosols in the mass-balance calculations.

These calculations were performed to provide a more nuanced understanding of soil forming processes and improve our interpretations of MAP proxy results. TiO_2 vs. ZrO_2 plots indicate both sandstones and mudstones are potential parent materials (Figure 7). However, the unweathered mudstones tend to have higher values of Al and Fe oxides (between 6 and 14 wt %) than the paleosols (between 4 and 10 wt %), leading to mass-balance calculations indicative of extremely weathered soils, which do not match our field observations (Tables 2 and S3). The very fine sandstones contain slightly more ZrO_2 by weight percent than the mudstones, suggesting a concentration of zircon minerals in the sand-sized fraction (Stiles et al., 2003). These results suggest that the true parent material may be a mixture of mudstone and sandstone but based on this evidence we conclude that the very fine sandstones are the best matching parent materials available.

TiO_2 is generally preferred as the immobile element for mass-balance geochemistry calculations because it is more abundant than ZrO_2 (wt % vs ppm), resulting in lower relative error (Driese et al., 2016). Therefore, TiO_2 was chosen as the immobile index element. The Wasatch Formation very fine sandstone at 153.3 m was chosen as the parent material for all mass-balance calculations because the Green River Formation very fine sandstone at 441.5 m resulted mass-balance enrichments of up to 600% that indicate an unrealistic amount of weathering for these paleosols based on our field observations (Figure 7 and Table S3). Using a single parent material for more than 900 m of stratigraphy is not ideal; however, thin section inspection of the sandstones indicates consistent mineralogy (Dickinson et al., 2012). The selection of coarser parent material (very fine sandstone) in comparison to the paleosols (very fine sandstone to siltstone) may affect the results of elements related to the translocation of clay, but clay-rich paleosols (Pedotype D) are rare and distributed evenly throughout the section. Therefore, we do not expect these decisions to introduce any systematic biases into our calculations.

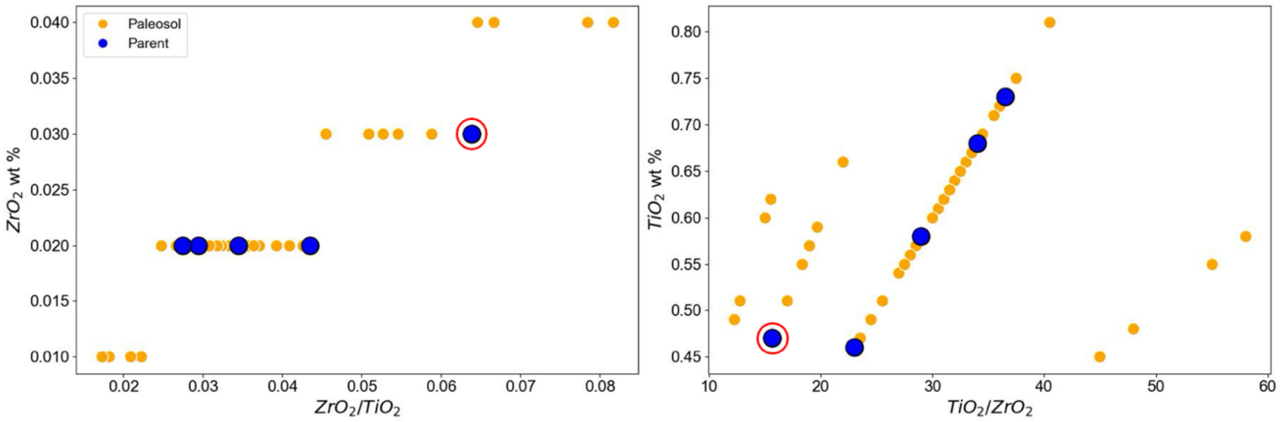

Figure 7: ZrO_2 vs. TiO_2 plots for the Wasatch and Green River Formation paleosols and potential parent materials. The chosen parent material (very fine sandstone from the Wasatch Formation) used in the mass-balance calculations is circled in red. Ideally, the best matching parent material should plot similarly, or be slightly lower, in the wt % of immobile elements compared to the paleosol samples.

https://doi.org/10.5194/egusphere-2026-1804
Preprint. Discussion started: 4 May 2026

3.4.2 Mass-balance results

The results of the mass-balance calculations are shown in Figure 8. A vertical line at zero indicates no gains or losses of an element relative to the parent material. A horizontal line at 395 m marks the Wasatch-Green River Formation contact. We grouped elements, which respond similarly to soil-forming processes, into three categories: 1) clay illuviation (Na_2O, K_2O, Al_2O_3, and SiO_2; Figure 8a), 2) redox-sensitive elements (Fe_2O_3 and Cr_2O_3; Figure 8b), and 3) calcium carbonate formation (MgO, CaO, and SrO; Figure 8c) (Ashley and Driese, 2000; Brantley et al., 2007). The redox-sensitive elements are helpful for determining the paleohydrology and water table fluctuations. MgO can either be grouped with calcium carbonate elements or clay elements in depositional systems with abundant Mg-rich smectite (Beverly et al., 2014); however, our results indicate that MgO best tracks calcium carbonate formation.

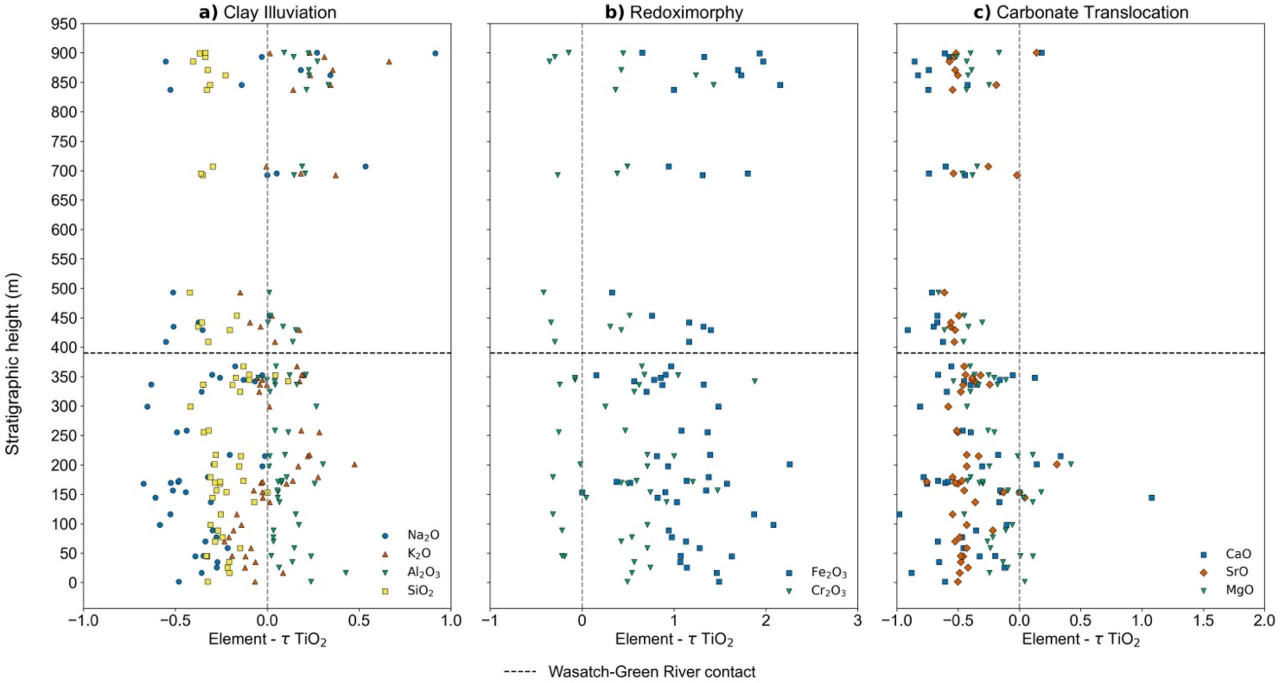

Figure 8: Mass-balance results with elements characteristic of a) clay illuviation (Na, K, Al, and Si) interpreted as precipitation intensity, b) redox-sensitive elements (Fe and Cr) interpreted as precipitation intermittency, and c) carbonate translocation (Ca, Sr, and Mg) interpreted as precipitation intermittency. The horizontal dashed line corresponds to the boundary between the Wasatch and Green River Formations, and the vertical dashed line at zero indicates no gains or losses of a mobile element relative to the parent material.

Figure 8a shows high clay illuviation, tracked primarily by K_2O and Al_2O_3, throughout the Wasatch and Green River Formations, particularly between 160 m and 350 m, near the end of the Wasatch Formation. The oxides tracking clay illuviation are close to 0% in the lower Green River Formation but are enriched between 25 and 50% in the middle Green

https://doi.org/10.5194/egusphere-2026-1804
Preprint. Discussion started: 4 May 2026

River Formation. Na_2O is weathered relatively quickly from soils (Sheldon et al., 2002) and thus, records consistent losses throughout the study section that are increased during the NCIEs. Surprisingly, SiO_2 shows no trend throughout the section with consistent losses of around 25%.

Based on the extent of enrichment, the redox-responsive elements indicate oxidizing conditions throughout the stratigraphy (Figure 8b). The paleosols are generally enriched in Fe_2O_3 and Cr_2O_3 throughout the entire section, with enrichments of 100 to 200% Fe_2O_3 and >50% Cr_2O_3. The trends in the redox-responsive elements are similar to the clay accumulation, which increases up to 200% at 125 m and persists with enrichments of ~150% until the top of the Wasatch Formation at 350 m. The redox-state of the paleosols around 700 m returns to values similar to values below 200 m (late Paleocene) (Figures 5b and 8b). Carbonate translocation in the Wasatch and Green River paleosols consistently records background losses of ~50% with larger losses up to 90% when redox-responsive and clay accumulation elements increase (Figure 8c), namely 160 m and 300 m in the Wasatch Formation, and throughout the Green River Formation from 400 to 900 m.

4 Discussion

4.1 Pedotype relationship to climate

Previous research shows that soil formation in the floodplain deposits of fluvial fans may change down-fan as fan toes are potentially closer to the water table (Plink-Björklund, 2021; Weissmann et al., 2013). This could result in misinterpretations of paleosol morphology and geochemistry due to local hydrological conditions as climate rather than a function of their position within the fan system (Ashley and Driese, 2000; Jenny, 1941). However, prior work shows no systematic downstream increase in soil moisture in the Uinta Basin fluvial fans. Although paleosols tend to be more reduced adjacent to channels and there are a greater proportion of floodplain deposits down-fan, no downstream changes in paleosol morphology, such as more reduced paleosols, were observed (Golab, 2010; Slawson et al., 2025b; Wang and Plink-Bjorklund, 2019). Based on this, we interpret the observed changes in paleosol geochemistry and morphology to be primarily a function of climate.

The presence of red matrix colors indicates that the paleosols in Pedotype A were well to moderately well drained with evapotranspiration outweighing precipitation (Kraus et al., 2013; Schwertmann, 1993; Vepraskas et al., 1993) and precipitation seasonality due to presence of vertic structures. Modern Vertisols form in seasonally wet and dry soil moisture conditions, leading to the shrinking and swelling of smectite clays that form slickensides (Scheffe et al., 2015). However, the zones of blue-gray depletion indicate periodic water saturation and are interpreted as root traces, based on the downward-tapering structure and tendency for depletion to occur adjacent to water-saturated rooting structures (Kraus and Hasiotis, 2006). Taken together, Pedotype A paleosols are paleo-Vertisols formed in oxidizing conditions with a seasonal change in soil moisture.

Pedotypes B and C have little evidence of pedogenesis beyond weak horizonation and ped structures. The red soil color observed in Pedotypes B and C, and the carbonate nodules in Pedotype C, are indicative of oxidized, well drained conditions (Schwertmann, 1993). Modern Inceptisols form in a variety of environments and climates across the globe today with minor horizon development (Scheffe et al., 2015).

Despite a greater abundance of clay, soil characteristics of Pedotype D are not significantly more mature than the other pedotypes. The higher proportion of clay reflects parent material rather than soil development. The gray-brown matrix colors indicates of moderately drained conditions compared to Pedotypes A to C (Beverly et al., 2018; Kraus et al., 2013; Vepraskas et al., 1993). The soil classification as a paleo-Inceptisol is not particularly informative for climatic interpretation since they form across the globe today in a variety of environments with poorly developed soils (Scheffe et al., 2015).

The carbonate nodules and deep red color indicates that Pedotype E was well drained (Schwertmann, 1993) and experienced primarily oxidizing condition, but the yellow-brown FeMn nodules found in these paleosols form due to fluctuating soil moisture conditions (Kraus et al., 2013; Macedo and Bryant, 1989). Pedotype E is indicative of dry, oxidizing conditions with perhaps higher amplitude fluctuations in the water table than Pedotypes A-D. Similar to the other paleo-Inceptisol pedotypes, the soil classification does not enable further climatic interpretation based on modern analogues due to its immature nature and presence across the globe today.

Pedotypes F and G are deep red, indicating generally well-drained, oxidizing conditions (Schwertmann, 1993), but differ from the other pedotypes with gleyed horizons at the base and top of the paleosols. The gleying at the base of the paleosols is interpreted to reflect groundwater processes (Duchaufour, 2012), but gleying at the top of the paleosols is likely due to anoxic conditions during river channel reoccupation (Driese and Ober, 2005; Kraus, 1999), known as “pseudogley” to distinguish it from water table saturation (Beverly et al., 2018). These paleosols are commonly found underneath channel or crevasse-splay deposits where water flowing through the river would be expected to interact with the buried paleosols, forming a reducing environment. We interpret the gleying of Pedotypes F and G to indicate a higher groundwater table unique to the Green River Formation, as they were not observed in the Wasatch Formation. Pedotypes F and G are indicative of oxidizing conditions with seasonal variations in soil moisture. This is especially true for the paleo-Vertisol, Pedotype G (Scheffe et al., 2015).

Overall, Pedotypes A through G are relatively immature and contain features indicating dry, oxidizing conditions. Slickensides, redoximorphic features, and FeMn nodules are indicative of seasonality and soil moisture fluctuations (Beverly et al., 2018; Kraus, 1999; Schwertmann, 1993).

4.2 Hyperthermal identification

With the chronology and five-point rolling average, we identify 11 NCIEs potentially representing hyperthermals in this 900 m section (Figure 9b). We use the naming conventions and ages of hyperthermals from Westerhold et al. (2018). Although hyperthermals are defined by paired negative carbon and oxygen isotope excursions of greater than one standard deviation in marine sediments (Kirtland Turner et al., 2014), bulk organic carbon isotope records in terrestrial environments are highly variable (Baczynski et al., 2013). Therefore, we identify NCIEs based on the presence of prominent peaks of greater than or equal to 1.5‰ in the five-point rolling average and age compared to Westerhold et al. (2018).

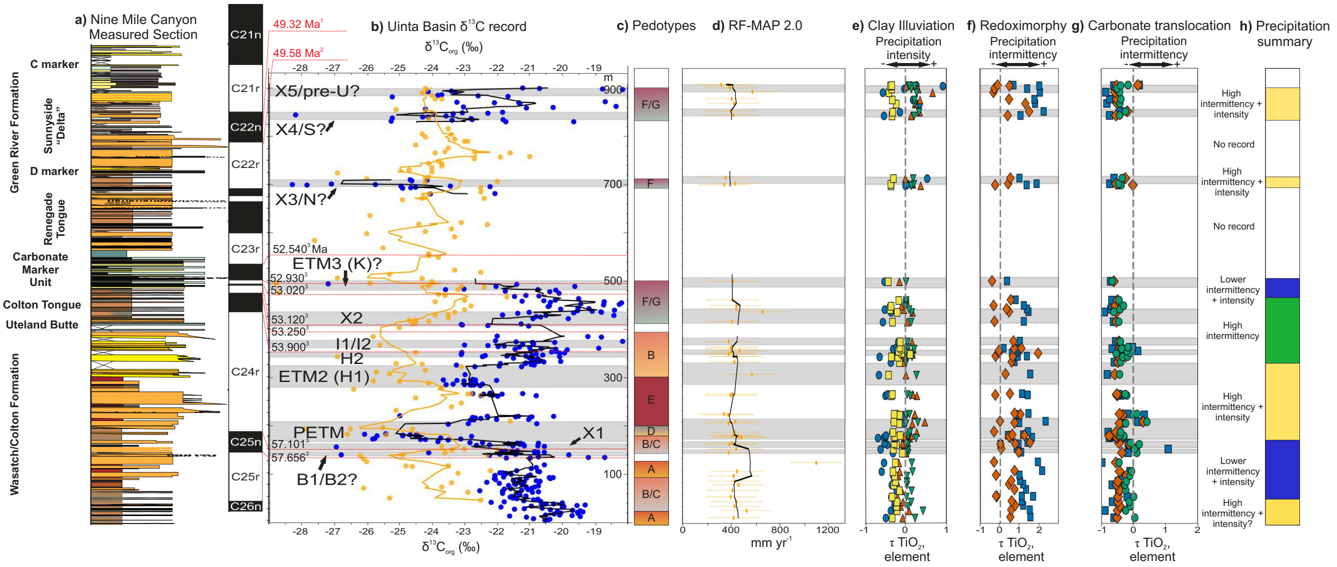

Figure 9: Summary figure containing all the paleoclimate data from this study. a) Measured section and geochronology from Nine Mile Canyon with superscripts corresponding to the sources described in Figures 1 and 5. b) Stable carbon isotope results from the Uinta Basin with a five-point rolling average. Hyperthermals denoted by gray shading. Data from this study is shown in blue and data from lacustrine Green River Formation (Birgenheier et al., 2020) shown in yellow. c) Simplified stratigraphic section with pedotype distribution. d) RF-MAP 2.0 mean annual precipitation results. e) Simplified summary of precipitation intermittency and intensity interpreted based on the paleosol mass balance results.

We identify one late Paleocene hyperthermal during Chron 25n (Ogg, 2020). The B1 and B2 hyperthermals occurred between 57.4 to 57.2 Ma (Figure 5a) and coincide with an excursion from -20.5‰ to -22.5‰ and a maximum negative value of -26.79‰ (Figure 9b). We identify this excursion as either B1 or B2, or both hyperthermals. Our geochronology does not allow us to differentiate between B1 and B2, which hereafter we refer to as B1/B2. B1/B2 are followed by an unidentified NCIE immediately preceding the PETM. This excursion, hereafter referred to as "X1", is marked by a shift from -21.5‰ to -23‰ and a maximum negative value of -26.7‰. Due to chronological constraints, we cannot determine which excursion this pre-PETM onset excursion corresponds to (Bowen et al., 2015).

The PETM is identified near the base of C24r as a 4‰ NCIE from background values of -21‰ to -25‰ (Figure 9b) (Slawson et al., 2025b). Both ETM2 (H1) and H2 hyperthermals are identified at the end of C24r (Figure 9b). The ETM2 excursion of -23‰ is muted in comparison to the PETM with a NCIE between 1‰ and 2‰. Following ETM2, baseline conditions return to -20.5‰. Similar to ETM2, H2 is marked by a muted NCIE of ~1.5‰. The next NCIE of ~2‰ is identified as the I1 and/or I2 hyperthermals (hereafter I1/I2), which we cannot differentiate with the current geochronology.

An unnamed NCIE, hereafter referred to as "X2," is the first excursion identified within the Colton Tongue of the Green River Formation (Figures 1 and 2). This excursion corresponds to a similar excursion in the Westerhold et al. (2018) record with a similar magnitude as events I1/I2, shifting from -20‰ to -22‰ (Figures 5a and 9b). In addition, the top of the Colton Tongue contains the base of ETM3 (K) hyperthermal before transitioning into lacustrine facies in the Carbonate Marker Unit. The ETM3 excursion in the Colton Tongue ranges from -21‰ to -22.8‰ with a maximum of -27.19‰; however, the entirety of the hyperthermal may not captured be captured, due to a lithology change in the Carbonate Marker Unit, which contains no paleosols for comparison.

Although we identify additional hyperthermals, we could not correlate them to named hyperthermals (e.g. Westerhold et al., 2018) due the lack of age control in the middle section of the Green River Formation. The absolute ages from the C marker and Mahogany Interval and the magnetostratigraphy in the Carbonate Marker Unit constrain the hyperthermals to 52.54 to 49.58 Ma, but further age constraint is not possible. Our first unnamed hyperthermal in the Green River Formation (X3) is marked by a dramatic NCIE of 3.5‰, from -24‰ to -27.5‰ (Figure 9b). However, the full hyperthermal may not captured here because this section of the stratigraphy is dominated by channel sandstones that could not be used for this analysis (Figure 9a).

No data is available between 725 and 850 m due to covered section and amalgamated channel sandstones without paleosols. We identify two more NCIEs in the Green River Formation (X4 and X5) between 825 and 855 m and 880 and 890 m, respectively (Figure 9b). The X4 excursion reaches a maximum of -25‰ from baseline values around -22.5‰, indicating a 2.5‰ excursion. The X5 excursion is similar, reaching a maximum of -24‰ and representing a 3‰ excursion. Overall, through analysis of floodplain organic carbon isotopes, previously published geochronology data (Slawson et al., 2025b), and comparison to marine carbon isotope curves, we identify 11 NCIEs in the Wasatch and Green River Formations representing up to 11 hyperthermals.

4.3 Mean annual precipitation proxy comparison

All MAP proxies show similar trends when errors are considered. RF-MAP 2.0 is most sensitive to CaO, TiO_2, and MgO, and although CaO (wt %) differs between hyperthermal paleosols and baseline paleosols, TiO_2 and MgO do not (Table S3). As a result, MAP changes are more muted than other proxies. In contrast, CIA-K, which is dependent on changes in wt % Na_2O and CaO (Sheldon et al., 2002), shows greater losses of CaO and Na_2O during hyperthermals than baseline paleosols (Figure 8 and Table S3). Although $PPM_{1.0}$ uses the same oxides (with the addition of Zr) as RF-MAP 2.0, $PPM_{1.0}$ it is more dependent on Na_2O, K_2O, Fe_2O_3, and TiO_2 than RF-MAP 2.0 (Lukens et al., 2019; Stinchcomb et al., 2016). $PPM_{1.0}$ does not

https://doi.org/10.5194/egusphere-2026-1804
Preprint. Discussion started: 4 May 2026

estimate a large increase in MAP for the paleosol near 115 m because it is not as dependent on CaO as RF-MAP 2.0 and CIA-K (Table S3). Because RF-MAP 2.0 is the most recent model with a larger database of modern soils and produces results with the lowest RMSPE, the remainder of our discussion uses reconstructed values from RF-MAP 2.0, although all values are available in Table S2.

4.4 Mass-balance interpretations

Overall, the paleosol morphology, such as red coloration and carbonate nodules (Figure 4), and MAP reconstruction for the early Paleogene indicate an arid to semiarid environment (441 ± 30 mm yr^{-1}) (Figure 9c and 9d), which is supported by the mass-balance geochemistry. The losses of CaO, SrO, and MgO in the paleosols are also indicative of an arid environment with fluctuating water tables (Ashley and Driese, 2000; Beverly et al., 2018). Dry and warm conditions, would be expected to lead to a lower and/or seasonally fluctuating water table, commonly associated with carbonate leaching and reprecipitation. In dry conditions, the leached carbonates rapidly become supersaturated in solution and reprecipitate as carbonate nodules (Breecker et al., 2009; Wieder & Yaalon, 1982). The accumulation of up to 200% more redox-sensitive elements relative to the parent material during the early Paleogene is also indicative of oxidizing and dry conditions.

Arid conditions also lead to a lower and/or more highly fluctuating water table, causing the decreased mobility and leaching of redox-sensitive elements under oxidizing conditions (Beverly et al., 2014, 2018). There are slight increases in the redox-sensitive elements during 8 of 11 hyperthermals except for I1/I2, H2, and ETM2 (Figure 9f). This increase indicates more oxidizing conditions, which we interpret to be a function of shorter wet seasons and/or greater evaporation rates in the absence of MAP change, during these extreme warming events.

The average loss of ~35% SiO_2 throughout the section is surprising, given the immobility of Si in soils except in very wet or low pH conditions (Stinchcomb et al., 2016; White et al., 2008). The loss of SiO_2 and Na_2O indicates the breakdown of sodium-bearing feldspars like albite (White et al., 2008). Although dissolved Si tends to be reincorporated into clay minerals (Chamley, 1989), moderate losses may track transport out of the system in solution (Stinchcomb et al., 2016). Furthermore, the illuviation of clay minerals could explain the loss of SiO_2 and Na_2O via hydrolysis of feldspars like plagioclase, while Al_2O_3 and K_2O results track increased clay illuviation via physical weathering. This discrepancy between elemental translocation of Si and Na versus Al and K could be further resolved by more detailed studies of the clay mineralogy and petrography of the paleosols in future work.

Soil geochemistry is also sensitive to changes in parent material and time forming on the landscape; however neither of these variables were observed to change throughout the section (e.g. (Slawson et al., 2025b). Temperature likely increased chemical weathering and evaporation rates (Gibson et al., 2000; Tateo, 2020), but cannot account for the high rates of clay illuviation. Instead, increased clay illuviation was likely driven by increased intensity of extreme precipitation events capable of enhanced erosion and infiltration of clay particles into the soil column (Ji et al., 2023; Slawson et al., 2025b). In addition, evidence of fluctuating redoximorphic conditions and increased loss of carbonates, indicating a seasonally variable water table, support our interpretation of less frequent, more intense extreme precipitation events with an overall constant

MAP. This interpretation is supported by the prevalence of upper flow regime structures indicative of flash flood events throughout the sandstones of the Wasatch and Green River Formations (Birgenheier et al., 2020; Gall et al., 2017; Plink-Björklund et al., 2014; Wang and Plink-Björklund, 2020). Previous work on ichnofossils of the Wasatch and Green River Formations report traces of ant nests, indicating seasonally low water tables, and *Steinichnus* ichnofacies, indicating high water tables, suggesting seasonal soil moisture extremes (Golab, 2010; Hasiotis, 2002). Other mid-latitude paleoclimate reconstructions at this time also document sedimentary evidence, such as upper flow regime structures, of high precipitation intensity and intermittency (Foreman et al., 2012, 2024; Schmitz and Pujalte, 2007; Slawson et al., 2025a; Zellman et al., 2020).

4.5 Precipitation change through the early Paleogene

High rates of clay illuviation, oxidizing conditions, and loss of carbonates prior to the PETM (Figure 9e-9g) are indicative of high precipitation intensity and intermittency prior to the PETM onset. High intensity precipitation has been invoked to as a consequence of the PETM in the Uinta and other mid-latitude basins (Foreman, 2014; Schmitz and Pujalte, 2007; Slawson et al., 2025b), but the length of this record allows us to make the observation that precipitation was already prone to high intensity and intermittency prior to the PETM. Rather than indicating a “state change” where mean annual precipitation decreased or shifted from more perennial to intermittent and intense at the PETM, we suggest the PETM represents an intensification of trends already present. This is further supported by the redox conditions, which were high throughout the late Paleocene with little response to the B1/B2 hyperthermals or the X1 NCIE (Figure 9f). However, redox conditions became even more oxidizing during the PETM, indicating that the water table was low but fluctuating enough to dissolve carbonates (Figure 9f and 9g).

Further describing pre-PETM precipitation results, due to the lack of an association with a NCIE in our record, the anomalously wet paleosol at 115 m may be an erroneous result. Such a rapid increase and decrease in MAP with no onset or offset is unusual as the NCIE record shows these excursions occurred over several paleosols; however, we cannot rule out that the result is at least in part related to MAP increase. This paleosol was exposed beneath a large, amalgamated channel sandstone complex. Water flowing through the overlying channel could have resulted in weathering the paleosol out of equilibrium with climate (Stinchcomb et al., 2016). Alternatively, the paleosol could have been exposed at the surface for an anomalously long period of time due to a pause in deposition, which could also lead to disequilibrium with climate (Stinchcomb et al., 2016). Because the paleosol does not show pseudogleying at the top, the second hypothesis is the more likely of the two. This abrupt change in MAP roughly lines up with unnamed NCIEs prior to Chron C25n in Westerhold et al. (2018) (Figure 5a); however, this NCIE is not identified in our $\delta^{13}C_{org}$ results (Figure 9b).

Of the overlying hyperthermals, only ETM2 and X2 indicate slightly higher MAP, but all are within error (Figure 9d). Post-PETM section, from 205-275 m, indicates a similar MAP to the PETM, ~400 mm yr^{-1}, and persistently high clay illuviation and redoximorphy, suggesting high intensity precipitation and shorter wet seasons (Figure 9d,e,f). In contrast, the carbonate translocation values returned to pre-PETM conditions at 220 m. Post-PETM, the fluvial stratigraphy indicates intense, intermittent precipitation (upper flow regime structures and amalgamated channel sandstones), continued for another 70 m after the PETM recovery (Figure 9a) (Slawson et al., 2025b). The onset of less amalgamated channel sandstones and lower clay illuviation and redoximorphy, indicating lower precipitation intermittency and intensity, correspond to the ETM2 recovery at 330 m (Figure 9a). The persistence of highly intermittent and intense precipitation despite a decrease in temperatures between the PETM and ETM2, at least on a global scale, highlight the presence of inertia and non-linearities in the Earth system, likely related to persistent change in precipitation systems due to the extreme warmth of the PETM (Piedrahita et al., 2024; Slawson et al., 2025b).

ETM2 was followed by a thin interval of fluvial deposits before the onset of H2 and I1/I2 (Figure 9a). The mass-balance and MAP values for H2 through ETM3 return to values in the late Paleocene, indicating a weaker response to warming than during the PETM and ETM2. Sea surface temperatures varied drastically on a global scale in their response to the early Paleogene hyperthermals (Lauretano et al., 2015; Westerhold et al., 2018). However, terrestrial temperature change during hyperthermals other than PETM is poorly resolved and currently only available from the Bighorn Basin (Snell et al., 2013). It is possible that the response to hyperthermal events was not uniform in western North America and that smaller temperature responses during hyperthermal events other than the PETM generate a smaller precipitation and weathering response.

The X3 through X5 NCIEs in the middle Green River Formation exhibit similar mass-balance and MAP results to the PETM and ETM2 (Figure 9d-9g). We interpret X3 to X5 to have static MAP but increased temperatures and precipitation intensity and intermittency due to observed mass balance changes in clay illuviation, redoximorphy, and carbonate translocation, and the abundance of upper flow regime sedimentary structures.

Higher intensity precipitation is expected to increase sediment transport and thus fluvial fan progradation (Carraro et al., 2023; Foreman, 2014; Pujalte et al., 2022; Zellman et al., 2023). Previous work proposed that fluvial deposition in the Uinta basin correlates with hyperthermals (Birgenheier et al., 2020), and lacustrine deposition correlates with non-hyperthermal periods in the Green River Formation (Birgenheier et al., 2020; Melstrom and Birgenheier, 2021). Our record supports this interpretation in some cases, as the middle Green River fluvial deposits are marked by the X3 through X5 excursions (Figure 9a and 9b). However, ETM3 was not associated with increased precipitation intensity in this record and appears to have started just prior to deposition of the lacustrine Carbonate Marker Unit (Figure 9b), suggesting that the responses of both the depositional systems and precipitation to warming may not be linear (Carmichael et al., 2018; Foreman et al., 2012; Piedrahita et al., 2024; Slawson et al., 2025b, a). Furthermore, the lack of samples from the lacustrine units results in a sampling bias towards the fluvial portions of the system; samples could not be collected from the lacustrine units to reliably identify hyperthermals due to internal carbon cycling in lacustrine systems (Bowen et al., 2008).

In conclusion, this record contributes to the small but increasing number of basins that record the terrestrial response to the lower magnitude Eocene hyperthermals (Abels et al., 2016; Chen et al., 2014; Honegger et al., 2020; Hyland et al., 2013), indicating the potential for fluvial environments to record high-resolution paleoclimate changes. Contrary to other Laramide Basins (Abels et al., 2016; Hyland et al., 2017; Kraus et al., 2013), the early Paleogene hyperthermals did not result in significant changes in MAP in the Uinta Basin. However, the hyperthermals, especially the PETM and ETM2, coincide with increases in precipitation intensity and a shorter wet season (Figure 9). These changes in precipitation intensity and intermittency persisted from the PETM through the ETM2, but were not as pronounced during some of the lower magnitude hyperthermals such as H2 and I1/I2, suggesting non-linearity and highly spatially dependent response of the Earth system to these global warming events (Honegger et al., 2020; Piedrahita et al., 2024). These complexities highlight the need for more spatially and temporally continuous multi-proxy datasets to more fully understand the effects of hyperthermals on precipitation.

4.6 Unnamed negative carbon isotope excursions

In an attempt to identify the X3-X5 events in the absence of high-resolution age model, the sedimentation rate between the bottom of Chrons C23r and C22n (Figure 9b), identified based on an absolute age date (Smith & Carroll, 2015), was calculated. We did not attempt to identify X1 and X2 in the same manner due to the lack of global, named NCIEs in these sections (e.g. Westerhold et al., 2018). While the current age controls do not support the assumption of a linear sedimentation rate (Figure 9a and 9b), this calculation is done simply as a rough estimate. Deposition of approximately 400 m between 52.54 and 49.58 Ma results in a sedimentation rate of 135 m/My. Accordingly, X3, X4, and X5 began around 51.49 Ma, 50.44 Ma, and 50.07 Ma, and each lasted approximately 150,000 Ky. Based on the dates provided in Westerhold et al. (2018), this age model suggests that X3 corresponds to the N hyperthermal, X4 to the S hyperthermal, and X5 to a pre-U NCIE (Figure 5a and 5b).

We compare our results to the stable carbon isotope record based on bulk organic matter from Birgenheier et al. (2020), also collected in Nine Mile Canyon, plotted in yellow in Figure 9b using a five-point rolling average. The record from Birgenheier et al. (2020) fills in some of the gaps from 500-700 m and 720-830 m (Figure 9b). The records show strong agreement through the H1 excursion near 320 m (Figure 9b). However, the Birgenheier et al. (2020) record alone would not result in the identification of H2, X4, or X5, and the I1/I2 hyperthermal is marked by a broader peak continuing higher in the stratigraphy. This may be due to the lower sample resolution, reworking of old carbon via sediment transport processes, or microbial activity that can differ from one site to another (Baczynski et al., 2013). Furthermore, there is a systematic shift to the right, towards isotopically heavier values, in our record compared to Birgenheier et al. (2020). This systematic shift is likely a result of the corrections that were made to our values based on the results of in-house standards run at the same time and does not impact the identification of hyperthermals.

4.7 Regional comparison of carbon isotope excursions and precipitation

4.7.1 Negative carbon isotope excursions

The $\delta^{13}C_{BOM}$ record presented here indicates that this method can be used to identify lower magnitude hyperthermals in fluvial environments. However, it also emphasizes the importance of a high-resolution age model given the often noisy and muted signal (Figure 9b). This is particularly the case for the ETM2, H2, and I1/I2 hyperthermals where the NCIEs are not nearly as negative as the other hyperthermals and there is little if any return to baseline values between the excursions (Figure 9b). The noisiness and muted response of the record is likely a function of local factors like vegetation change, microbial activity, or reworking of old carbon (Arens et al., 2000; Foreman et al., 2024; Kohn, 2010). Floodplain deposition is also inherently dynamic as a function of river position and flood frequency, where some sections are likely to not record the entirety of the hyperthermals, contributing to the lack of a return to baseline values, a muted isotope record, or simply missing peak excursion values.

Other records of early Paleogene hyperthermals in similar sedimentary basins commonly rely on the carbon isotope values of carbonate nodules instead of bulk organic matter to avoid the problems of reworked carbon (e.g. Abels et al., 2016; Bowen & Bowen, 2008; Hyland et al., 2013; Schmitz & Pujalte, 2007). Although pedogenic carbonate nodules are preferred to study carbon cycling (Abels et al., 2016; Honegger et al., 2020), they are not found in every paleosol in the Uinta Basin, limiting their utility.

One trend identified in this organic carbon isotope record and nearly ubiquitous in similar terrestrial and marine records is the long term shift to more negative carbon isotope values in the peak of the EECO (53.26-49.14 Ma) (Figure 9b) (Lauretano et al., 2018; Westerhold et al., 2018). This signal is not present in our record from the I1/I2 through ETM3 hyperthermals, but we find the most negative $\delta^{13}C_{BOM}$ values (down to -29.20‰) in the ETM3 through S excursions (Figure 9b).

4.7.2 Regional hydroclimatic response to hyperthermals

The suggested changes in mean annual precipitation during the PETM and subsequent Eocene hyperthermals in other Laramide basins are varied and incomplete with some records indicating slight drying (Bataille et al., 2019; Kraus et al., 2013; Zellman et al., 2020, 2023), wetting (Foreman et al., 2012), or no response (Abels et al., 2016; Wilf, 2000). Many of the recorded MAP increases or decreases are within the reported errors of the proxy models, indicating that the lack of a change in MAP in our record may not be anomalous. The most robust response of hydroclimate in the mid-latitudes to the early Paleogene hyperthermals is an increase in the intensity of precipitation (Foreman, 2014; Foreman et al., 2012, 2024; Payros et al., 2022; Pujalte et al., 2015), which our results support for the PETM, ETM2, and some of the other lower magnitude Eocene NCIEs.

In a warming climate, precipitation extremes are driven by both the thermodynamic response (Held and Soden, 2006) and the dynamical response that is often altered over land, potentially resulting in super-Clausius-Clapeyron scaling (Bao et al., 2017; Byrne and O'Gorman, 2015; Carmichael et al., 2018; Lenderink et al., 2017; Slawson et al., 2025a). This dynamical response may be non-linear in these sustained, extremely warm Paleogene climates, resulting in prolonged hydroclimate change locally to regionally despite a decrease in temperature globally (Slawson et al., 2025b, a). This record, particularly changes during the PETM and ETM2, support this hypothesis given the persistence of increased precipitation intensity and intermittency evidenced by 1) increased accumulation of redox-sensitive elements and clay illuviation (Figure

9e and 9f), and 2) abundance of upper flow regime sedimentary structures throughout the stratigraphy (Birgenheier et al., 2020; Melstrom and Birgenheier, 2021; Plink-Björklund et al., 2014). However, this interpretation is complicated by a lack of proxies that can quantitatively measure precipitation intensity and seasonality. The continued expansion of high-resolution records in terrestrial environments is paramount for further testing this hypothesis.

The currently limited record of precipitation change during the early Paleogene hyperthermals records indicate wetting in more northern Laramide basins (Abels et al., 2016; Hyland et al., 2013) and aridification, potentially related more to changing precipitation extremes and seasonality than MAP, in southern basins (Bowen and Bowen, 2008; Kelson et al., 2018; Zellman et al., 2020). This pattern may indicate a poleward shift in global circulation, and the subtropical jet and storm tracks, similarly predicted for future climate (Reichler, 2016; Tierney et al., 2022; Zhang et al., 2024).

4.8 Paleoclimate model comparison

To test the paleoclimate model community's understanding on these extremely warm climates, we compare our proxy record to the DeepMIP ensemble results using the newly available web-based application, which converts modern latitude and longitude to the paleo-location (Table 2 and S4) (Steinig et al., 2024). A latitude-longitude of 39.8, -110.3 was used as the modern location of Nine Mile Canyon, where our samples were collected (Figure 1). CO_2 estimates for this time period have considerable uncertainty (Lunt et al., 2017; The Cenozoic CO Proxy Integration Project (CenCOPIP) Consortium*† et al., 2023; Wang et al., 2020). We use the parameters provided in Lunt et al. (2017) to select CO_2 concentrations representative of the late Paleocene, PETM, post-PETM, and EECO (Table 2 and S4). For the late Paleocene and post-PETM, the 3x CO_2 concentration (840 ppm) was used. For the PETM and EECO, the 6xCO_2 concentration (1680 ppm) was used. We also calculated the monsoon precipitation index (MPI) (Wang & Ding, 2008) to estimate the model ensemble's precipitation variability for comparison to the seasonal nature of precipitation revealed in this proxy record and others (Birgenheier et al., 2020; Carraro et al., 2023; Melstrom & Birgenheier, 2021; Wang & Plink-Bjorklund, 2019). The high precipitation intermittency and intensity in this record is supported by regional climate modeling that shows the Uinta basin was arid (0-360 mm yr^{-1}) and received most of the annual precipitation from a summer monsoon (Sewall and Sloan, 2006).

The formula for MPI is,

$$\boldsymbol{MPI} = (\boldsymbol{summer\ precipitation} - \boldsymbol{winter\ precipitation}) \div \boldsymbol{annual\ precipitation} \tag{2}$$

where MPI > 0.5 and a summer-wet and winter-dry hydroclimate indicates monsoon-derived moisture sources and a seasonally variable hydroclimate. The precipitation estimates provided by the DeepMIP web application are in mm day^{-1} and we calculated MAP by multiplying by 365. The standard deviations of the model precipitation estimates were calculated based on the individual model outputs (Steinig et al., 2024). Following Wang and Ding (2008), we computed the annual range of precipitation by summing the summer (MJJAS) and winter (NDJFM) precipitation and calculating the difference (Table S4).

https://doi.org/10.5194/egusphere-2026-1804
Preprint. Discussion started: 4 May 2026

Table 2. Atmospheric CO_2 concentrations and the correspondingly selected DeepMIP model ensemble results from Steinig et al. (2024). The monsoon precipitation index (MPI) was calculated using the formula from Wang and Ding (2008) to estimate precipitation variability.

Time periods	**Model CO_2** (ppm)	**Model**	**Model MAP ± SD (mm yr^{-1})**	**Proxy MAP ± SE (mm yr^{-1})**	**Model summer precipitation (mm)**	**Model winter precipitation (mm)**	**MPI**
Late Paleocene, Post-PETM	840 (3x CO_2)	ensemble mean	803±175	441±30	564	132	0.54
PETM, EECO	1680 (6x CO_2)	ensemble mean	949±214	441±30	669	129	0.56

Our analysis shows a poor agreement between the DeepMIP MAP and this proxy record even after accounting for the RMSPE of RF-MAP 2.0 (±209 mm **yr^{-1}**) (Table 2). Modeled MAP is >350 mm yr^{-1} higher than proxy reconstructed MAP during the Paleocene and post-PETM and >500 mm yr^{-1} higher during the PETM and EECO (Table 2). MPI ranges from 0.5 to 0.6 regardless of the CO_2 concentration, indicating moderate precipitation variability (Table 2). If the Sewall and Sloan (2003) regional model and our proxy-based interpretations are correct, MPI should be closer to 1.0 because of the proxy evidence for extreme wet and dry seasons (Birgenheier et al., 2020; Melstrom and Birgenheier, 2021; Plink-Björklund et al., 2014). Although the DeepMIP model overestimates MAP, the model results indicate a summer-wet climate for all of the selected time periods, suggesting monsoon-derived precipitation (Table S4).

Global climate models are run at a coarse resolution, and thus have difficulty realistically representing precipitation in complex terrain (Rahimi et al., 2024; Rummukainen, 2010), such as the Rocky Mountain West. In addition, global climate models struggle to simulate extreme precipitation events (Birgenheier et al., 2020; Foreman et al., 2012, 2024; Rahimi et al., 2024; Rummukainen, 2010). Updated regional climate models in the Rocky Mountain West run during the early Paleogene hyperthermals would be beneficial for further understanding the drivers of spatial shifts in precipitation, changes in precipitation intensity and seasonality, and future precipitation change in this region. Importantly, climate models need to be tested with the paleoclimate data from the mid-latitudes to understand the discrepancies between their results and the proxy estimated MAP and seasonal precipitation. Additional data is needed on boundary conditions to accurately represent these extreme climates both in the past and future.

5 Conclusions

Using bulk stable carbon isotope methods, we identify 11 hyperthermals from the late Paleocene and early Eocene in the Uinta Basin using NCIEs from floodplain bulk organic matter. Paleosol major element geochemistry and changes in fluvial sedimentology indicate a decoupling of extreme precipitation from MAP during hyperthermals in the Uinta Basin. Our paleosol-based proxy record suggests that MAP remained constant at 441 ± 30 mm yr^{-1}, but both temperature and precipitation intensity increased, leading to shorter wet seasons and changes in soil formation, especially during the PETM and ETM2. This was reflected by consistent MAP estimates and mass-balance geochemistry changes related to weathering process such as clay illuviation, accumulation of redox-sensitive elements, and carbonate translocation. Comparison of our proxy record to the DeepMIP model ensemble indicates MAP 400 to 500 mm yr^{-1} higher than our proxy reconstructions. In addition, sedimentary structures identified in the Uinta Basin indicate much greater seasonality of precipitation, both in intensity and intermittency than identified in the DeepMIP model - both of which require future investigation.

Code and data availability

The data presented in this study are available at Zenodo (doi:10.5281/zenodo.19408468) and in a tabular format in the supplementary material (Slawson et al., 2026)

Supplement link

Author contributions

Conceptualization: JSS, PPB; Methodology: JSS, PPB, EJB; Investigation: JSS, PPB, EJB; Visualization: JSS, PPB, EJB; Funding acquisition: JSS, PPB; Project administration: JSS, PPB; Supervision: PPB; Writing – original draft: JSS; Writing – review & editing: JSS, PPB, EJB.

Competing interests

Authors declare that they have no competing interests.

Disclaimer

Acknowledgements

We acknowledge the analytical contributions of the CU Boulder Earth Systems Stable Isotope Lab (CUBES-SIL) Core Facility (RRID:SCR_019300). We would also like to thank Liran Dor and Dorian Gurtsky for their assistance collecting samples in the field.

Financial support

Colorado Mountain Club Foundation Fellowship (no grant ID number).
Colorado Scientific Society Student Research Grant (no grant ID number).

Review statement

The review statement will be added by Copernicus Publications listing the handling editor as well as all contributing referees according to their status anonymous or identified.

References

Abels, H. A., Lauretano, V., van Yperen, A. E., Hopman, T., Zachos, J. C., Lourens, L. J., Gingerich, P. D., and Bowen, G. J.: Environmental impact and magnitude of paleosol carbonate carbon isotope excursions marking five early Eocene hyperthermals in the Bighorn Basin, Wyoming, Clim. Past, 12, 1151–1163, https://doi.org/10.5194/cp-12-1151-2016, 2016.

Anderson, S., Dietrich, W., and Brimhall, G.: Weathering profiles, mass-balance analysis, and rates of solute loss: Linkages between weathering and erosion in a small, steep catchment, Bull. Geol. Soc. Am., 114, https://doi.org/10.1130/0016-7606(2002)114%253C1143:WPMBAA%253E2.0.CO, 2002.

Arens, N. C., Jahren, A. H., and Amundson, R.: Can C3 plants faithfully record the carbon isotopic composition of atmospheric carbon dioxide?, Paleobiology, 26, 137–164, https://doi.org/10.1666/0094-8373(2000)026%253C0137:CCPFRT%253E2.0.CO;2, 2000.

Ashley, G. M. and Driese, S. G.: Paleopedology and Paleohydrology of a Volcaniclastic Paleosol Interval: Implications for Early Pleistocene Stratigraphy and Paleoclimate Record, Olduvai Gorge, Tanzania, J. Sediment. Res., 70, 1065–1080, https://doi.org/10.1306/040300701065, 2000.

Baczynski, A. A., McInerney, F. A., Wing, S. L., Kraus, M. J., Bloch, J. I., Boyer, D. M., Secord, R., Morse, P. E., and Fricke, H. C.: Chemostratigraphic implications of spatial variation in the Paleocene-Eocene Thermal Maximum carbon isotope excursion, SE Bighorn Basin, Wyoming, Geochem. Geophys. Geosystems, 14, 4133–4152, https://doi.org/10.1002/ggge.20265, 2013.

Bao, J., Sherwood, S. C., Alexander, L. V., and Evans, J. P.: Future increases in extreme precipitation exceed observed scaling rates, Nat. Clim. Change, 7, 128–132, https://doi.org/10.1038/nclimate3201, 2017.

Bataille, C. P., Ridgway, K. D., Colliver, L., and Liu, X.-M.: Early Paleogene fluvial regime shift in response to global warming: A subtropical record from the Tornillo Basin, west Texas, USA, GSA Bull., 131, 299–317, https://doi.org/10.1130/B31872.1, 2019.

Beverly, E. and Plink-Bjorklund, P.: Supporting information for: Long-Term Decoupling of Precipitation Extremes from Mean Annual Precipitation During Repeated Early Paleogene Hyperthermals in the North American Mid-Latitudes (1), https://doi.org/10.5281/ZENODO.19405866, 2026.

Beverly, E. J., Ashley, G. M., and Driese, S. G.: Reconstruction of a Pleistocene paleocatena using micromorphology and geochemistry of lake margin paleo-Vertisols, Olduvai Gorge, Tanzania, Quat. Int., 322–323, 78–94, https://doi.org/10.1016/j.quaint.2013.10.005, 2014.

Beverly, E. J., Lukens, W. E., and Stinchcomb, G. E.: Paleopedology as a tool for reconstructing paleoenvironments and paleoecology, in: Vertebrate Paleobiology and Paleoanthropology, Springer, 151–183, https://doi.org/10.1007/978-3-319-94265-0_9, 2018.

Birgenheier, L. P., Berg, M. D. V., Plink-Björklund, P., Gall, R. D., Rosencrans, E., Rosenberg, M. J., Toms, L. C., and Morris, J.: Climate impact on fluvial-lake system evolution, Eocene Green River Formation, Uinta Basin, Utah, USA, Bull. Geol. Soc. Am., 132, 562–587, https://doi.org/10.1130/B31808.1, 2020.

Bowen, G. J. and Bowen, B. B.: Mechanisms of PETM global change constrained by a new record from central Utah, Geology, 36, 379–382, https://doi.org/10.1130/G24597A.1, 2008.

Bowen, G. J., Daniels, A. L., and Bowen, B. B.: Paleoenvironmental Isotope Geochemistry and Paragenesis of Lacustrine and Palustrine Carbonates, Flagstaff Formation, Central Utah, U.S.A., J. Sediment. Res., 78, 162–174, https://doi.org/10.2110/jsr.2008.021, 2008.

Bowen, G. J., Maibauer, B. J., Kraus, M. J., Röhl, U., Westerhold, T., Steimke, A., Gingerich, P. D., Wing, S. L., and Clyde, W. C.: Two massive, rapid releases of carbon during the onset of the Palaeocene-Eocene thermal maximum, Nat. Geosci., 8, https://doi.org/10.1038/NGEO2316, 2015.

Brantley, S. L. and Lebedeva, M.: Learning to Read the Chemistry of Regolith to Understand the Critical Zone, Annu. Rev. Earth Planet. Sci., 39, 387–416, https://doi.org/10.1146/annurev-earth-040809-152321, 2011.

Brantley, S. L., Goldhaber, M. B., and Ragnarsdottir, K. V.: Crossing Disciplines and Scales to Understand the Critical Zone, Elements, 3, 307–314, https://doi.org/10.2113/gselements.3.5.307, 2007.

Brimhall, G. H. and Dietrich, W. E.: Constitutive mass balance relations between chemical composition, volume, density, porosity, and strain in metasomatic hydrochemical systems: Results on weathering and pedogenesis, Geochim. Cosmochim. Acta, 51, 567–587, https://doi.org/10.1016/0016-7037(87)90070-6, 1987.

Burke, K. D., Williams, J. W., Chandler, M. A., Haywood, A. M., Lunt, D. J., and Otto-Bliesner, B. L.: Pliocene and Eocene provide best analogs for near-future climates., Proc. Natl. Acad. Sci. U. S. A., 115, 13288–13293, https://doi.org/10.1073/pnas.1809600115, 2018.

Byrne, M. P. and O'Gorman, P. A.: The Response of Precipitation Minus Evapotranspiration to Climate Warming: Why the "Wet-Get-Wetter, Dry-Get-Drier" Scaling Does Not Hold over Land, Am. Meteorol. Soc., 2015.

Carmichael, M. J., Inglis, G. N., Badger, M. P. S., Naafs, B. D. A., Behrooz, L., Remmelzwaal, S., Monteiro, F. M., Rohrssen, M., Farnsworth, A., Buss, H. L., Dickson, A. J., Valdes, P. J., Lunt, D. J., and Pancost, R. D.: Hydrological and associated biogeochemical consequences of rapid global warming during the Paleocene-Eocene Thermal Maximum, Glob. Planet. Change, 157, 114–138, https://doi.org/10.1016/j.gloplacha.2017.07.014, 2017.

Carmichael, M. J., Pancost, R. D., and Lunt, D. J.: Changes in the occurrence of extreme precipitation events at the Paleocene–Eocene thermal maximum, Earth Planet. Sci. Lett., 501, 24–36, https://doi.org/10.1016/j.epsl.2018.08.005, 2018.

Carraro, D., Ventra, D., and Moscariello, A.: Anatomy of a fluvial paleo-fan: sedimentological and architectural trends of the Paleocene–Eocene Wasatch–Colton System (western Uinta Basin, Utah, U.S.A.), J. Sediment. Res., 93, 370–412, https://doi.org/10.2110/jsr.2022.095, 2023.

Chamley, H.: Clay Sedimentology, Springer, Berlin, Heidelberg, https://doi.org/10.1007/978-3-642-85916-8, 1989.

Chen, Z., Ding, Z., Tang, Z., Wang, X., and Yang, S.: Early Eocene carbon isotope excursions: Evidence from the terrestrial coal seam in the Fushun Basin, Northeast China, Geophys. Res. Lett., 41, 3559–3564, https://doi.org/10.1002/2014GL059808, 2014.

Cramer, B. S., Wright, J. D., Kent, D. V., and Aubry, M.: Orbital climate forcing of δ^{13}C excursions in the late Paleocene–early Eocene (chrons C24n–C25n), Paleoceanography, 18, 2003PA000909, https://doi.org/10.1029/2003PA000909, 2003.

Cramwinckel, M. J., Burls, N. J., Fahad, A. A., Knapp, S., West, C. K., Reichgelt, T., Greenwood, D. R., Chan, W.-L., Donnadieu, Y., Hutchinson, D. K., de Boer, A. M., Ladant, J.-B., Morozova, P. A., Niezgodzki, I., Knorr, G., Steinig, S., Zhang, Z., Zhu, J., Feng, R., Lunt, D. J., Abe-Ouchi, A., and Inglis, G. N.: Global and Zonal-Mean Hydrological Response to Early Eocene Warmth, Paleoceanogr. Paleoclimatology, 38, e2022PA004542, https://doi.org/10.1029/2022PA004542, 2023.

Dickinson, W. R., Klute, M. A., Hayes, M. J., Janecke, S. U., Lundin, E. R., McKITTRICK, M. A., and Olivares, M. D.: Paleogeographic and paleotectonic setting of Laramide sedimentary basins in the central Rocky Mountain region, Geol. Soc. Am. Bull., 100, 1023–1039, https://doi.org/10.1130/0016-7606(1988)100%253C1023:PAPSOL%253E2.3.CO;2, 1988.

Dickinson, W. R., Lawton, T. F., Pecha, M., Davis, S. J., Gehrels, G. E., and Young, R. A.: Provenance of the Paleogene Colton Formation (Uinta Basin) and Cretaceous–Paleogene provenance evolution in the Utah foreland: Evidence from U-Pb ages of detrital zircons, paleocurrent trends, and sandstone petrofacies, 2012.

Dittus, A. J., Karoly, D. J., Lewis, S. C., and Alexander, L. V.: A Multiregion Assessment of Observed Changes in the Areal Extent of Temperature and Precipitation Extremes, J. Clim., 28, 9206–9220, https://doi.org/10.1175/JCLI-D-14-00753.1, 2015.

Donat, M. G., Angélil, O., and Ukkola, A. M.: Intensification of precipitation extremes in the world's humid and water-limited regions, Environ. Res. Lett., 14, 065003, https://doi.org/10.1088/1748-9326/ab1c8e, 2019.

Driese, S. G. and Ober, E. G.: Paleopedologic and Paleohydrologic Records of Precipitation Seasonality from Early Pennsylvanian "Underclay" Paleosols, U.S.A., J. Sediment. Res., 75, 997–1010, https://doi.org/10.2110/jsr.2005.075, 2005.

Duchaufour, R.: Pedology: Pedogenesis and classification, Springer Science & Business Media, 476 pp., 2012.

Foreman, B. Z.: Climate-driven generation of a fluvial sheet sand body at the Paleocene–Eocene boundary in north-west Wyoming (USA), Basin Res., 26, 225–241, https://doi.org/10.1111/bre.12027, 2014.

Foreman, B. Z., Heller, P. L., and Clementz, M. T.: Fluvial response to abrupt global warming at the Palaeocene/Eocene boundary, Nature, 491, 92–95, https://doi.org/10.1038/nature11513, 2012.

Foreman, B. Z., Secord, R., and Korasidis, V. A.: The Paleocene-Eocene Thermal Maximum Recognized in Distal Alluvial Fan Strata of the Sevier Fold-And-Thrust Belt (Southwestern Wyoming, USA), Paleoceanogr. Paleoclimatology, 39, e2024PA004959, https://doi.org/10.1029/2024PA004959, 2024.

Fouch, T., Hanley, J., Forester, R., Keighin, C., Pitman, J., and Nichols, D.: Chart showing lithology, mineralogy, and paleontology of the nonmarine North Horn Formation and Flagstaff Member of the Green River Formation, Price Canyon, central Utah: a principal reference section, https://doi.org/10.3133/i1797A, 1987.

Fouch, T. D.: Lithofacies and related hydrocarbon accumulations in Tertiary strata of the western and central Uinta Basin, Utah, in: Rocky Mountain Association of Geologists, Symposium, Rocky Mountain Association of Geologists, 163–173, 1975.

Fouch, T.D., Nuccio, V. F., Anders, D. E., Rice, D. D., Pitman, J. K., and Mast, R. F.: Green River (!) Petroleum System, Uinta Basin, Utah, U.S.A., in: The petroleum system—From source to trap, vol. 60, American Association of Petroleum Geologists, 399–421, 1994.

Gall, R. D., Birgenheier, L. P., and Vanden Berg, M. D.: Highly Seasonal and Perennial Fluvial Facies: Implications For Climatic Control On the Douglas Creek and Parachute Creek Members, Green River Formation, Southeastern Uinta Basin, Utah, U.S.A., J. Sediment. Res., 87, 1019–1047, https://doi.org/10.2110/jsr.2017.54, 2017.

Gibson, T. G., Bybell, L. M., and Mason, D. B.: Stratigraphic and climatic implications of clay mineral changes around the Paleocene/Eocene boundary of the northeastern US margin, Sediment. Geol., 134, 65–92, https://doi.org/10.1016/S0037-0738(00)00014-2, 2000.

Golab, J. A.: Ichno-Pedological Facies of the Colton and Lower-Middle Green River Formations: Implications for Continental Paleoclimate Studies, M.S., Colorado School of Mines, United States -- Colorado, 118 pp., 2010.

Hasiotis, S. T.: Continental Ichnology: Using Terrestrial and Freshwater Trace Fossils for Environmental and Climatic Interpretations, in: Continental Trace Fossils, vol. 51, edited by: Hasiotis, S. T., SEPM Society for Sedimentary Geology, 0, https://doi.org/10.2110/scn.06.51.0001, 2002.

Hayden, F. V.: Preliminary Field Report of the United States Geological Survey of Colorado and New Mexico, Annual Report, Government Printing Office, https://doi.org/10.3133/70038884, 1869.

Held, I. M. and Soden, B. J.: Robust Responses of the Hydrological Cycle to Global Warming, J. Clim., 19, 5686–5699, https://doi.org/10.1175/JCLI3990.1, 2006.

Honegger, L., Adatte, T., Spangenberg, J. E., Caves Rugenstein, J. K., Poyatos-Moré, M., Puigdefàbregas, C., Chanvry, E., Clark, J., Fildani, A., Verrechia, E., Kouzmanov, K., Harlaux, M., and Castelltort, S.: Alluvial record of an early Eocene hyperthermal within the Castissent Formation, the Pyrenees, Spain, Clim. Past, 16, 227–243, https://doi.org/10.5194/cp-16-227-2020, 2020.

Hyland, E., Sheldon, N. D., and Fan, M.: Terrestrial paleoenvironmental reconstructions indicate transient peak warming during the early Eocene climatic optimum, Bull. Geol. Soc. Am., 125, 1338–1348, https://doi.org/10.1130/B30761.1, 2013.

Hyland, E. G., Sheldon, N. D., and Cotton, J. M.: Constraining the early Eocene climatic optimum: A terrestrial interhemispheric comparison, Bull. Geol. Soc. Am., 129, 244–252, https://doi.org/10.1130/B31493.1, 2017.

Hyland, E. G., Huntington, K. W., Sheldon, N. D., and Reichgelt, T.: Temperature seasonality in the North American continental interior during the Early Eocene Climatic Optimum, Clim. Past, 14, 1391–1404, https://doi.org/10.5194/cp-14-1391-2018, 2018.

Inglis, G. N., Bragg, F., Burls, N. J., Cramwinckel, M. J., Evans, D., Foster, G. L., Huber, M., Lunt, D. J., Siler, N., Steinig, S., Tierney, J. E., Wilkinson, R., Anagnostou, E., de Boer, A. M., Dunkley Jones, T., Edgar, K. M., Hollis, C. J., Hutchinson, D. K., and Pancost, R. D.: Global mean surface temperature and climate sensitivity of the early Eocene Climatic Optimum (EECO), Paleocene–Eocene Thermal Maximum (PETM), and latest Paleocene, Clim. Past, 16, 1953–1968, https://doi.org/10.5194/cp-16-1953-2020, 2020.

Jenny, H.: Factors of soil formation: a system of quantitative pedology., McGraw Hill book company, Inc., 1941.

Ji, K., Wang, C., Hong, H., Yin, K., Zhao, C., Xu, Y., Song, B., Prins, M., Lourens, L. J., Gingerich, P. D., and Abels, H. A.: Elevated physical weathering exceeds chemical weathering of clays during the Paleocene-Eocene Thermal Maximum in the continental Bighorn Basin (Wyoming, USA), Palaeogeogr. Palaeoclimatol. Palaeoecol., 615, 111445, https://doi.org/10.1016/j.palaeo.2023.111445, 2023.

Jones, E. R.: PROBABILISTIC SOURCE-TO-SINK ANALYSIS OF THE PROVENANCE OF THE CALIFORNIA PALEORIVER: IMPLICATIONS FOR THE EARLY EOCENE PALEOGEOGRAPHY OF WESTERN NORTH AMERICA, 2017.

Kelson, J. R., Watford, D., Bataille, C., Huntington, K. W., Hyland, E., and Bowen, G. J.: Warm Terrestrial Subtropics During the Paleocene and Eocene: Carbonate Clumped Isotope (Δ47) Evidence From the Tornillo Basin, Texas (USA), Paleoceanogr. Paleoclimatology, 33, 1230–1249, https://doi.org/10.1029/2018PA003391, 2018.

Kirtland Turner, S., Sexton, P. F., Charles, C. D., and Norris, R. D.: Persistence of carbon release events through the peak of early Eocene global warmth, Nat. Geosci., 7, 748–751, https://doi.org/10.1038/ngeo2240, 2014.

Kohn, M. J.: Carbon isotope compositions of terrestrial C3 plants as indicators of (paleo)ecology and (paleo)climate, Proc. Natl. Acad. Sci., 107, 19691–19695, https://doi.org/10.1073/pnas.1004933107, 2010.

Könitzer, S. F., Leng, M. J., Davies, S. J., and Stephenson, M. H.: An assessment of geochemical preparation methods prior to organic carbon concentration and carbon isotope ratio analyses of fine-grained sedimentary rocks, Geochem. Geophys. Geosystems, 13, 2012GC004094, https://doi.org/10.1029/2012GC004094, 2012.

Kraus, M. J.: Paleosols in clastic sedimentary rocks: their geologic applications, Earth-Science Reviews, 1999.

Kraus, M. J. and Hasiotis, S. T.: Significance of Different Modes of Rhizolith Preservation to Interpreting Paleoenvironmental and Paleohydrologic Settings: Examples from Paleogene Paleosols, Bighorn Basin, Wyoming, U.S.A., J. Sediment. Res., 76, 633–646, https://doi.org/10.2110/jsr.2006.052, 2006.

Kraus, M. J., McInerney, F. A., Wing, S. L., Secord, R., Baczynski, A. A., and Bloch, J. I.: Paleohydrologic response to continental warming during the Paleocene-Eocene Thermal Maximum, Bighorn Basin, Wyoming, Palaeogeogr. Palaeoclimatol. Palaeoecol., 370, 196–208, https://doi.org/10.1016/j.palaeo.2012.12.008, 2013.

Lauretano, V., Littler, K., Polling, M., Zachos, J. C., and Lourens, L. J.: Frequency, magnitude and character of hyperthermal events at the onset of the Early Eocene Climatic Optimum, Clim. Past, 11, 1313–1324, https://doi.org/10.5194/cp-11-1313-2015, 2015.

Lauretano, V., Zachos, J. C., and Lourens, L. J.: Orbitally Paced Carbon and Deep-Sea Temperature Changes at the Peak of the Early Eocene Climatic Optimum, Paleoceanogr. Paleoclimatology, 33, 1050–1065, https://doi.org/10.1029/2018PA003422, 2018.

Lenderink, G., Barbero, R., Loriaux, J. M., and Fowler, H. J.: Super-Clausius–Clapeyron Scaling of Extreme Hourly Convective Precipitation and Its Relation to Large-Scale Atmospheric Conditions, https://doi.org/10.1175/JCLI-D-16-0808.1, 2017.

Littler, K., Röhl, U., Westerhold, T., and Zachos, J. C.: A high-resolution benthic stable-isotope record for the South Atlantic: Implications for orbital-scale changes in Late Paleocene–Early Eocene climate and carbon cycling, Earth Planet. Sci. Lett., 401, 18–30, https://doi.org/10.1016/j.epsl.2014.05.054, 2014.

Lukens, W. E., Stinchcomb, G. E., Nordt, L. C., Kahle, D. J., Driese, S. G., and Tubbs, J. D.: Recursive partitioning improves paleosol proxies for rainfall, Am. J. Sci., 319, 819–845, https://doi.org/10.2475/10.2019.01, 2019.

Lunt, D. J., Huber, M., Anagnostou, E., Baatsen, M. L. J., Caballero, R., DeConto, R., Dijkstra, H. A., Donnadieu, Y., Evans, D., Feng, R., Foster, G. L., Gasson, E., Von Der Heydt, A. S., Hollis, C. J., Inglis, G. N., Jones, S. M., Kiehl, J., Kirtland Turner, S., Korty, R. L., Kozdon, R., Krishnan, S., Ladant, J.-B., Langebroek, P., Lear, C. H., LeGrande, A. N., Littler, K., Markwick, P., Otto-Bliesner, B., Pearson, P., Poulsen, C. J., Salzmann, U., Shields, C., Snell, K., Stärz, M., Super, J., Tabor, C., Tierney, J. E., Tourte, G. J. L., Tripati, A., Upchurch, G. R., Wade, B. S., Wing, S. L., Winguth, A. M. E., Wright, N. M., Zachos, J. C., and Zeebe, R. E.: The DeepMIP contribution to PMIP4: experimental design for model simulations of the EECO, PETM, and pre-PETM (version 1.0), Geosci. Model Dev., 10, 889–901, https://doi.org/10.5194/gmd-10-889-2017, 2017.

Lunt, D. J., Bragg, F., Chan, W.-L., Hutchinson, D. K., Ladant, J.-B., Morozova, P., Niezgodzki, I., Steinig, S., Zhang, Z., Zhu, J., Abe-Ouchi, A., Anagnostou, E., De Boer, A. M., Coxall, H. K., Donnadieu, Y., Foster, G., Inglis, G. N., Knorr, G., Langebroek, P. M., Lear, C. H., Lohmann, G., Poulsen, C. J., Sepulchre, P., Tierney, J. E., Valdes, P. J., Volodin, E. M., Dunkley Jones, T., Hollis, C. J., Huber, M., and Otto-Bliesner, B. L.: DeepMIP: model intercomparison of early Eocene climatic optimum (EECO) large-scale climate features and comparison with proxy data, Clim. Past, 17, 203–227, https://doi.org/10.5194/cp-17-203-2021, 2021.

Macedo, J. and Bryant, R. B.: Preferential Microbial Reduction of Hematite Over Goethite in a Brazilian Oxisol, Soil Sci. Soc. Am. J., 53, 1114–1118, https://doi.org/10.2136/sssaj1989.03615995005300040022x, 1989.

Mack, G. H., James, W. C., and Monger, H. C.: Classification of paleosols, Geol. Soc. Am. Bull., 105, 129–136, https://doi.org/10.1130/0016-7606(1993)105%253C0129:COP%253E2.3.CO;2, 1993.

Matthews, K. J., Maloney, K. T., Zahirovic, S., Williams, S. E., Seton, M., and Müller, R. D.: Global plate boundary evolution and kinematics since the late Paleozoic, Glob. Planet. Change, 146, 226–250, https://doi.org/10.1016/j.gloplacha.2016.10.002, 2016.

Maynard, J. B.: Chemistry of Modern Soils as a Guide to Interpreting Precambrian Paleosols, J. Geol., 100, 279–289, https://doi.org/10.1086/629632, 1992.

Mcinerney, F. A. and Wing, S. L.: The Paleocene-Eocene Thermal Maximum: A Perturbation of Carbon Cycle, Climate, and Biosphere with Implications for the Future INTRODUCTION AND BRIEF HISTORY OF STUDY, Annu. Rev. Earth Planet. Sci. Online Earthannualreviewsorg, 39, 489–516, https://doi.org/10.1146/annurev-earth-040610-133431, 2011.

Melstrom, E. M. and Birgenheier, L. P.: Stratigraphic architecture of climate influenced hyperpycnal mouth bars, Sedimentology, 68, 1580–1605, https://doi.org/10.1111/sed.12854, 2021.

Morgan, C. D.: Geologic guide and road logs of the Willow Creek, Indian, Soldier Creek, Nine Mile, Gate, and Desolation Canyons, Uinta Basin, Utah, Utah Geological Survey, Salt Lake City, Utah., 79 pp., 2003.

Munsell Color (Firm): Munsell soil color charts : with genuine Munsell color chips, 2009 year revised. Grand Rapids, MI : Munsell Color, 2010., 2010.

Myers, T., Tabor, N., and Rosenau, N.: Multiproxy approach reveals evidence of highly variable paleoprecipitation in the Upper Jurassic Morrison Formation (western United States), Geol. Soc. Am. Bull., 126, 1105–1116, https://doi.org/10.1130/B30941.1, 2014.

Ogg, J. G.: Chapter 5 - Geomagnetic Polarity Time Scale, in: Geologic Time Scale 2020, edited by: Gradstein, F. M., Ogg, J. G., Schmitz, M. D., and Ogg, G. M., Elsevier, 159–192, https://doi.org/10.1016/B978-0-12-824360-2.00005-X, 2020.

Payros, A., Pujalte, V. no, and Schmitz, B.: Mid-latitude alluvial and hydroclimatic changes during the Paleocene–Eocene Thermal Maximum as recorded in the Tremp-Graus Basin, Spain, Sediment. Geol., 435, https://doi.org/10.1016/j.sedgeo.2022.106155, 2022.

Piedrahita, V. A., Roberts, A. P., Rohling, E. J., Heslop, D., Zhao, X., Galeotti, S., Florindo, F., Grant, K. M., Hu, P., and Li, J.: Dry hydroclimates in the late Palaeocene-early Eocene hothouse world, Nat. Commun., 15, 7042, https://doi.org/10.1038/s41467-024-51430-6, 2024.

Plink-Björklund, P.: Distributive Fluvial Systems: Fluvial and Alluvial Fans, in: Encyclopedia of Geology, Elsevier, 745–758, https://doi.org/10.1016/b978-0-08-102908-4.00015-1, 2021.

Plink-Björklund, P., Birgeneier, L., and Jones, E.: Extremely bad early Eocene weather: Evidence for extreme precipitation from rived deposits, Rendiconti Online Della Soc. Geol. Ital., 31, 175–176, https://doi.org/10.3301/ROL.2014.107, 2014.

Pujalte, V., Baceta, J. I., and Schmitz, B.: A massive input of coarse-grained siliciclastics in the Pyrenean Basin during the PETM: The missing ingredient in a coeval abrupt change in hydrological regime, Clim. Past, 11, 1653–1672, https://doi.org/10.5194/cp-11-1653-2015, 2015.

Pujalte, V., Schmitz, B., and Payros, A.: A rapid sedimentary response to the Paleocene-Eocene Thermal Maximum hydrological change: New data from alluvial units of the Tremp-Graus Basin (Spanish Pyrenees), Palaeogeogr. Palaeoclimatol. Palaeoecol., 589, 110818–110818, https://doi.org/10.1016/j.palaeo.2021.110818, 2022.

Rahimi, S., Huang, L., Norris, J., Hall, A., Goldenson, N., Krantz, W., Bass, B., Thackeray, C., Lin, H., Chen, D., Dennis, E., Collins, E., Lebo, Z. J., Slinskey, E., Graves, S., Biyani, S., Wang, B., Cropper, S., and the UCLA Center for Climate Science Team: An overview of the Western United States Dynamically Downscaled Dataset (WUS-D3), Geosci. Model Dev., 17, 2265–2286, https://doi.org/10.5194/gmd-17-2265-2024, 2024.

Reichler, T.: Chapter 6 - Poleward Expansion of the Atmospheric Circulation, in: Climate Change (Second Edition), edited by: Letcher, T. M., Elsevier, Boston, 79–104, https://doi.org/10.1016/B978-0-444-63524-2.00006-3, 2016.

Remy, R., R.: Stratigraphy of the Eocene part of the Green River Formation in the south-central part of the Uinta Basin, Utah, https://doi.org/10.3133/b1787BB, 1992.

Retallack, G., JAMES, W., MACK, G., and Monger, C.: Classification of paleosols: Discussion and reply, Geol. Soc. Am. Bull. - GEOL SOC AMER BULL, 105, 1635–1637, 1993.

Rummukainen, M.: State-of-the-art with regional climate models, WIREs Clim. Change, 1, 82–96, https://doi.org/10.1002/wcc.8, 2010.

Scheffe, K., Shaw, J., Stolt, M., and Weindorf, D.: Illustrated Guide to Soil Taxonomy, version 2, US Dep. Agric. Nat. Resour. Conserv. Serv. Natl. Soil Surv. Cent. Linc. Neb., 2015.

Schmitz, B. and Pujalte, V.: Abrupt increase in seasonal extreme precipitation at the Paleocene-Eocene boundary, Geology, 35, 215–218, https://doi.org/10.1130/G23261A.1, 2007.

Schwertmann, U.: Relations Between Iron Oxides, Soil Color, and Soil Formation, in: Soil Color, John Wiley & Sons, Ltd, 51–69, https://doi.org/10.2136/sssaspecpub31.c4, 1993.

Sewall, J. O. and Sloan, L. C.: Come a little bit closer: A high-resolution climate study of the early Paleogene Laramide foreland, Geology, 34, 81, https://doi.org/10.1130/G22177.1, 2006.

Sheldon, N. D. and Tabor, N. J.: Quantitative paleoenvironmental and paleoclimatic reconstruction using paleosols, Earth-Sci. Rev., 95, 1–52, https://doi.org/10.1016/j.earscirev.2009.03.004, 2009.

Sheldon, N. D., Retallack, G. J., and Tanaka, S.: Geochemical Climofunctions from North American Soils and Application to Paleosols across the Eocene-Oligocene Boundary in Oregon, J. Geol., 110, 687–696, https://doi.org/10.1086/342865, 2002.

Slawson, J. S., Plink-Bjorklund, B. P., Reichler, T., and Baldassare, D.: More intermittent mid-latitude precipitation accompanied extreme early Palaeogene warmth, Nat. Geosci., https://doi.org/10.1038/s41561-025-01870-6, 2025a.

Slawson, J. S., Plink-Bjorklund, B. P., Beverly, E. J., and Bachtadse, V.: Paleosol-Based Reconstruction Indicates Decoupling of Mean Annual Precipitation and Precipitation Intensity During the Paleocene-Eocene Thermal Maximum in the Uinta Basin, Utah, Paleoceanogr. Paleoclimatology, 40, e2024PA004966, https://doi.org/10.1029/2024PA004966, 2025b.

Smith, F., Wing, S., and Freeman, K.: Magnitude of the carbon isotope excursion at the Paleocene–Eocene thermal maximum: The role of plant community change, Earth Planet. Sci. Lett., 262, 50–65, https://doi.org/10.1016/j.epsl.2007.07.021, 2007.

Smith, M. E. and Carroll, A. R. (Eds.): Stratigraphy and Paleolimnology of the Green River Formation, Western USA, Springer Netherlands, Dordrecht, https://doi.org/10.1007/978-94-017-9906-5, 2015.

Smith, M. E., Chamberlain, K. R., Singer, B. S., and Carroll, A. R.: Eocene clocks agree: Coeval 40Ar/39Ar, U-Pb, and astronomical ages from the Green River Formation, Geology, 38, 527–530, https://doi.org/10.1130/G30630.1, 2010.

Snell, K. E., Thrasher, B. L., Eiler, J. M., Koch, P. L., Sloan, L. C., and Tabor, N. J.: Hot summers in the Bighorn Basin during the early Paleogene, Geology, 41, 55–58, https://doi.org/10.1130/G33567.1, 2013.

Spieker, E. M.: Late Mesozoic and early Cenozoic history of central Utah, Prof. Pap., https://doi.org/10.3133/pp205D, 1946.

Steinig, S., Abe-Ouchi, A., De Boer, A. M., Chan, W.-L., Donnadieu, Y., Hutchinson, D. K., Knorr, G., Ladant, J.-B., Morozova, P., Niezgodzki, I., Poulsen, C. J., Volodin, E. M., Zhang, Z., Zhu, J., Evans, D., Inglis, G. N., Meckler, A. N., and Lunt, D. J.: DeepMIP-Eocene-p1: multi-model dataset and interactive web application for Eocene climate research, Sci. Data, 11, 970, https://doi.org/10.1038/s41597-024-03773-4, 2024.

Stiles, C. A., Mora, C. I., and Driese, S. G.: Pedogenic processes and domain boundaries in a Vertisol climosequence: evidence from titanium and zirconium distribution and morphology, Geoderma, 116, 279–299, https://doi.org/10.1016/S0016-7061(03)00105-8, 2003.

Stinchcomb, G. E., Nordt, L. C., Driese, S. G., Lukens, W. E., Williamson, F. C., and Tubbs, J. D.: A data-driven spline model designed to predict paleoclimate using paleosol geochemistry, Am. J. Sci., 316, 746–777, https://doi.org/10.2475/08.2016.02, 2016.

Tateo, F.: Clay Minerals at the Paleocene–Eocene Thermal Maximum: Interpretations, Limits, and Perspectives, Minerals, 10(12), 2020.

The Cenozoic CO Proxy Integration Project (CenCOPIP) Consortium*†, Hönisch, B., Royer, D. L., Breecker, D. O., Polissar, P. J., Bowen, G. J., Henehan, M. J., Cui, Y., Steinthorsdottir, M., McElwain, J. C., Kohn, M. J., Pearson, A., Phelps, S. R., Uno, K. T., Ridgwell, A., Anagnostou, E., Austermann, J., Badger, M. P. S., Barclay, R. S., Bijl, P. K., Chalk, T. B., Scotese, C. R., De La Vega, E., DeConto, R. M., Dyez, K. A., Ferrini, V., Franks, P. J., Giulivi, C. F., Gutjahr, M., Harper, D. T., Haynes, L. L., Huber, M., Snell, K. E., Keisling, B. A., Konrad, W., Lowenstein, T. K., Malinverno, A., Guillermic, M., Mejía, L. M., Milligan, J. N., Morton, J. J., Nordt, L., Whiteford, R., Roth-Nebelsick, A., Rugenstein, J. K. C., Schaller, M. F., Sheldon, N. D., Sosdian, S., Wilkes, E. B., Witkowski, C. R., Zhang, Y. G., Anderson, L., Beerling, D. J., Bolton, C., Cerling, T. E., Cotton, J. M., Da, J., Ekart, D. D., Foster, G. L., Greenwood, D. R., Hyland, E. G., Jagniecki, E. A., Jasper, J. P., Kowalczyk, J. B., Kunzmann, L., Kürschner, W. M., Lawrence, C. E., Lear, C. H., Martínez-Botí, M. A., Maxbauer, D. P., Montagna, P., Naafs, B. D. A., Rae, J. W. B., Raitzsch, M., Retallack, G. J., Ring, S. J., Seki, O., Sepúlveda, J., Sinha, A., Tesfamichael, T. F., Tripati, A., Van Der Burgh, J., Yu, J., Zachos, J. C., and Zhang, L.: Toward a Cenozoic history of atmospheric CO2, Science, 382, eadi5177, https://doi.org/10.1126/science.adi5177, 2023.

Tierney, J., Zhu, J., Li, M., Ridgwell, A., Hakim, G., Poulsen, C., Whiteford, R., Rae, J., and Kump, L.: Spatial patterns of climate change across the Paleocene-Eocene Thermal Maximum, Earth Atmospheric Planet. Sci., 119, https://doi.org/10.1073/pnas, 2022.

Tierney, J. E., Poulsen, C. J., Montañez, I. P., Bhattacharya, T., Feng, R., Ford, H. L., Hönisch, B., Inglis, G. N., Petersen, S. V., Sagoo, N., Tabor, C. R., Thirumalai, K., Zhu, J., Burls, N. J., Foster, G. L., Goddéris, Y., Huber, B. T., Ivany, L. C., Turner, S. K., Lunt, D. J., McElwain, J. C., Mills, B. J. W., Otto-Bliesner, B. L., Ridgwell, A., and Zhang, Y. G.: Past climates inform our future, Science, 370, https://doi.org/10.1126/science.aay3701, 2020.

Vepraskas, M. J., Wilding, L. P., and Drees, L. R.: Aquic conditions for Soil Taxonomy: concepts, soil morphology and micromorphology, in: Developments in Soil Science, vol. 22, edited by: Ringrose-Voase, A. J. and Humphreys, G. S., Elsevier, 117–131, https://doi.org/10.1016/S0166-2481(08)70402-1, 1993.

Wang, B. and Ding, Q.: Global monsoon: Dominant mode of annual variation in the tropics, Dyn. Atmospheres Oceans, 44, 165–183, https://doi.org/10.1016/j.dynatmoce.2007.05.002, 2008.

Wang, J. and Plink-Bjorklund, P.: Stratigraphic complexity in fluvial fans: Lower Eocene Green River Formation, Uinta Basin, USA, https://doi.org/10.1111/bre.12350, 2019.

Wang, J. and Plink-Björklund, P.: Variable-discharge-river macroforms in the Sunnyside Delta Interval of the Eocene Green River Formation, Uinta Basin, USA, Sedimentology, 67, 1914–1950, https://doi.org/10.1111/sed.12688, 2020.

Wang, Y., Wang, L., Momohara, A., Leng, Q., and Huang, Y.-J.: The Paleogene atmospheric CO2 concentrations reconstructed using stomatal analysis of fossil *Metasequoia* needles, Palaeoworld, 29, 744–751, https://doi.org/10.1016/j.palwor.2020.03.002, 2020.

Weissmann, G. S., Hartley, A. J., Scuderi, L. A., Nichols, G. J., Davidson, S. K., Owen, A., Atchley, S. C., Bhattacharyya, P., Chakraborty, T., Ghosh, P., Nordt, L. C., Michel, L., and Tabor, N. J.: Prograding distributive fluvial systems-geomorphic models and ancient examples, SEPM Spec. Publ., 104, 131–147, https://doi.org/10.2110/sepmsp.104.16, 2013.

Westerhold, T., Röhl, U., Donner, B., and Zachos, J. C.: Global Extent of Early Eocene Hyperthermal Events: A New Pacific Benthic Foraminiferal Isotope Record From Shatsky Rise (ODP Site 1209), Paleoceanogr. Paleoclimatology, 33, 626–642, https://doi.org/10.1029/2017PA003306, 2018.

Westerhold, T., Marwan, N., Drury, A. J., Liebrand, D., Agnini, C., Anagnostou, E., Barnet, J. S. K., Bohaty, S. M., De Vleeschouwer, D., Florindo, F., Frederichs, T., Hodell, D. A., Holbourn, A. E., Kroon, D., Lauretano, V., Littler, K., Lourens, L. J., Lyle, M., Pälike, H., Röhl, U., Tian, J., Wilkens, R. H., Wilson, P. A., and Zachos, J. C.: An astronomically dated record of Earth's climate and its predictability over the last 66 million years, Science, 369, 1383–1387, https://doi.org/10.1126/science.aba6853, 2020.

White, A. F., Schulz, M. S., Vivit, D. V., Blum, A. E., Stonestrom, D. A., and Anderson, S. P.: Chemical weathering of a marine terrace chronosequence, Santa Cruz, California I: Interpreting rates and controls based on soil concentration-depth profiles, Geochim. Cosmochim. Acta, 72, 36–68, https://doi.org/10.1016/j.gca.2007.08.029, 2008.

Wilf, P.: Late Paleocene–early Eocene climate changes in southwestern Wyoming: Paleobotanical analysis, Geol. Soc. Am. Bull., 2000.

Williams, C. J. R., Lunt, D. J., Salzmann, U., Reichgelt, T., Inglis, G. N., Greenwood, D. R., Chan, W., Abe-Ouchi, A., Donnadieu, Y., Hutchinson, D. K., Boer, A. M., Ladant, J., Morozova, P. A., Niezgodzki, I., Knorr, G., Steinig, S., Zhang, Z., Zhu, J., Huber, M., and Otto-Bliesner, B. L.: African Hydroclimate During the Early Eocene From the DeepMIP Simulations, Paleoceanogr. Paleoclimatology, 37, https://doi.org/10.1029/2022PA004419, 2022.

Zachos, J. C., Dickens, G. R., and Zeebe, R. E.: An early Cenozoic perspective on greenhouse warming and carbon-cycle dynamics, Nature, 451, 279–283, https://doi.org/10.1038/nature06588, 2008.

Zellman, K. L., Plink-Björklund, P., and Fricke, H. C.: Testing hypotheses on signatures of precipitation variability in the river and floodplain deposits of the paleogene san juan basin, New Mexico, U.S.A., J. Sediment. Res., 90, 1770–1801, https://doi.org/10.2110/JSR.2020.75, 2020.

Zellman, K. L., Plink-Björklund, P., and Spangler, L.: Progradational-to-retrogradational styles of Palaeogene fluvial fan successions in the San Juan Basin, New Mexico, Basin Res., bre.12823, https://doi.org/10.1111/bre.12823, 2023.

Zhang, X., Tipple, B. J., Zhu, J., Rush, W. D., Shields, C. A., Novak, J. B., and Zachos, J. C.: Response of coastal California hydroclimate to the Paleocene–Eocene Thermal Maximum, Clim. Past, 20, 1615–1626, https://doi.org/10.5194/cp-20-1615-2024, 2024.